applied sciences

MDPI

Article

Experimental Investigation of the Influence of Longitudinal Tilt Angles on the Thermal Performance of a Small-Scale Linear Fresnel Reflector

Carmen López-Smeetz [1], Arsenio Barbón [2], Luis Bayón [3,*] and Covadonga Bayón-Cueli [4]

[1] Polytechnic School of Engineering of Gijón, University of Oviedo, 33203 Asturias, Spain; uo231922@uniovi.es
[2] Department of Electrical Engineering, University of Oviedo, 33003 Oviedo, Spain; barbon@uniovi.es
[3] Department of Mathematics, University of Oviedo, 33003 Oviedo, Spain
[4] DNV UK Limited, Operating Expenses (OPEX), Aberdeen AB21 0BR, UK; covadonga.bayon.cueli@dnv.com
* Correspondence: bayon@uniovi.es

Abstract: This paper analyses the influence of the longitudinal tilt angle of the secondary system of a low-concentration photovoltaic system based on a small-scale linear Fresnel reflector. Several evaluation indicators, such as useful heat gain, thermal efficiency, incident solar irradiance gain on the photovoltaic cells, and total useful energy gain, were evaluated for five wind speed conditions and six locations in the Northern Hemisphere. The tests were performed with two small-scale linear Fresnel reflector configurations: the classical large-scale linear Fresnel reflector configuration (base configuration) and the optimal longitudinal tilt angle configuration (longitudinal tilt configuration). An experimental platform based on an open-loop wind tunnel was designed and built for this purpose. As far as useful heat production, the longitudinal tilt configuration performs worse as the longitudinal tilt angle and wind speed increase. A useful heat gain 33.91% lower than the base configuration is obtained with a wind speed of 10.03 (m/s) at the 36.86 (°) latitude location. Thermal efficiency decreases with increasing wind speed and longitudinal tilt angle. The thermal efficiency is between 0.3 and 0.2 with wind speeds of 4.99 (m/s) and 10.03 (m/s). The longitudinal tilt configuration shows the best increase in total useful energy gain in the absence of wind (up to 53% at a latitude of 36.86 (°)). This increase is 25% at this same location with a wind speed of 10.03 (m/s). It can be concluded that the effect of the longitudinal tilt of the secondary system has a positive effect. To highlight the importance of this work, the results obtained in the configuration comparison were used to compare a nonconcentrating photovoltaic system and a low-concentration photovoltaic system. The incident solar irradiance on the photovoltaic cells is much higher with nonconcentrating photovoltaic technology. This solar irradiance gain is over 60% for the base configuration and 45% for the longitudinal tilt configuration. The total useful energy gain is 70% in the absence of wind and at the 36.86 (°) latitude location in favour of the low-concentration photovoltaic system. The nonconcentrating photovoltaic system performs better with a wind speed of 10.03 (m/s).

Keywords: low-concentration photovoltaic system;small-scale linear Fresnel reflector; longitudinal tilt angle; wind speed; heat losses

check for updates

Citation: López-Smeetz, C.; Barbón, A.; Bayón, L.; Bayón-Cueli, C. Experimental Investigation of the Influence of Longitudinal Tilt Angles on the Thermal Performance of a Small-Scale Linear Fresnel Reflector. *Appl. Sci.* **2024**, *14*, 3666. https://doi.org/10.3390/app14093666

Academic Editor: Francesco Calise

Received: 12 March 2024
Revised: 21 April 2024
Accepted: 23 April 2024
Published: 25 April 2024

Copyright: © 2024 by the authors. Licensee MDPI, Basel, Switzerland. This article is an open access article distributed under the terms and conditions of the Creative Commons Attribution (CC BY) license (https://creativecommons.org/licenses/by/4.0/).

1. Introduction

The decarbonisation process endorsed by European Union (*EU*) countries in the 2015 Paris Agreement [1] was revalidated at the 2022 United Nations climate change conference in Cairo, Egypt, with more ambitious targets. Achieving these goals requires the use of renewable energies such as solar energy, wind energy, etc. Although global solar and wind electricity production in 2022 reached 1322.6 (TWh) and 2104.8 (TWh) [2], respectively, the level of renewable energy needed to mitigate climate change has not yet been reached. In 2022, photovoltaic (*PV*) power generation capacity was 1.05 (TW), while wind capacity was 0.89 (TW) [2]. These data confirm photovoltaic technology as one of the renewable

energy sources that will be able to replace fossil fuels given that this energy is clean, free, and unlimited.

Photovoltaic systems produce electricity directly and can be divided into two technologies: nonconcentrating photovoltaic systems ($NCPV$s) and concentrating photovoltaic systems (CPVs). In an $NCPV$ system, the PV cells receive nonconcentrating solar irradiance. These systems can use a solar tracking system or remain at a fixed tilt angle throughout the year. Solar tracking systems are classified according to their motion: (i) two rotation axes (dual-axis trackers) or (ii) a single rotation axis (single-axis trackers). Although dual-axis trackers generate the most power, single-axis trackers are the most widely used. In contrast, in a CPV system, optical devices (mirrors, lenses) concentrate the solar irradiance incident on the collector area into a much smaller area, achieving a significant increase in the flow of solar energy incident on the photovoltaic cells. These systems require a solar tracking system. Depending on the geometric concentration ratio (defined as the number of times solar irradiance is concentrated), expressed in number of suns (1 sun equals 1000 (W/m^2), CPV technology can be classified into [3] high-concentration photovoltaics ($HCPV$s) (between 100 suns and 1000 suns), medium-concentration photovoltaics ($MCPV$s) (between 10 suns and 100 suns), and low-concentration photovoltaics ($LCPV$s) (from 2 suns to 10 suns).

Some of the differences between concentrating and nonconcentrating systems are shown below:

(i) PV cell efficiency. $NCPV$ systems use commercial silicon cells with efficiencies between 10% and 20% [4]. In contrast, CPV systems use multijunction cells with an efficiency as high as 39% [4].

(ii) The solar tracking system. A solar tracking system is mandatory in a CPV system. However, solar tracking is optional in an $NCPV$ system even though the use thereof increases electricity production. The use of solar tracking systems in CPV and $NCPV$ systems complicates their implementation and increases their cost.

(iii) Incident solar irradiance on PV cells. The beam, diffuse, and ground-reflected components of solar irradiance are incident on the PV cells in $NCPV$ systems. In contrast, only the beam component is incident on the PV cells in CPV systems. The available diffuse solar irradiance often represents a significant fraction of the solar irradiance on a tilted surface. There are even some locations where this component is decisive.

(iv) The operating temperature of the PV cells. The energy production of a PV system depends on the operating temperature of the PV cells [5]. For example, manufacturers of crystalline photovoltaic cells estimate a decrease of between 0.4% and 0.65% in electrical efficiency per °C increase over the reference operating temperature [6]. In CPV systems, the concentration of solar irradiance causes an increase in the temperature of the PV cells, but it is easier to implement a cooling system due to the size of the PV cell system. In contrast, it is not possible to implement a cooling system in $NCPV$ system due to the large size of the PV cell system. In addition to reducing the electrical efficiency of PV cells, the high temperatures to which a PV cell system is subjected damage its backsheet, encapsulants, edge seals, and optical coatings [7].

(v) The system cost. Due to the low efficiency of PV cells, $NCPV$ systems require large PV cell surfaces. In contrast, CPV systems are equipped with cheaper optical materials (e.g., mirrors or lenses), which reduces the cost of these devices. Even so, it has been estimated that the cost of an $LCPV$ system can be more than double (2.3 times) the cost of an $NCPV$ system [8]. However, Moreno et al. [9] presented a study showing that under certain conditions ((i) high beam solar irradiance (>2.5 (MWh/m^2year)) and (ii) at utility scale) CPV technologies can be competitive with $NCPV$ systems.

(vi) Waste PV cells. The lifetime of PV modules is estimated at 25 years. PV modules must be recycled after this period. In its report [10], the International Energy Agency Photovoltaic Power Systems ($IEA-PVPS$) estimates that 1.7 million tonnes of PV modules will need to be recycled by 2030 and 60 million tonnes by 2050. CPV systems use a fraction of the PV cell surface area that $NCPV$ systems use, so the resulting

waste in *CPV* systems will also be a fraction. This is one of the main advantages of *CPV* systems.

(vii) The cogeneration system. Cogeneration systems are a very important element nowadays in reducing global warming [11]. Both thermal energy and electrical energy are necessary in the building sector. *CPV* systems can produce heat and electricity simultaneously, for increased efficiency, whereas *NCPV* systems can only produce electrical energy.

(viii) The surface area required for system implementation. The deployment of *PV* technologies in buildings is limited by the available surface area on building roofs. Silva and Fernandes [12] presented a study showing that *LCPV* systems require 60% less surface area to produce the same thermal and electrical performance compared to the combined use of flat thermal and *NCPV* systems.

The traditional concentrators used in *CPV* systems are (i) parabolic trough concentrators, (ii) parabolic dish concentrators, and (iii) linear Fresnel reflectors. Concentrators (i) and (ii) use curved reflecting surfaces [13], resulting in a low level of uniformity in the illumination of the *PV* cells and, therefore, a noticeable decrease in the electrical efficiency of the *PV* cells. In contrast, linear Fresnel reflectors can be equipped with flat mirrors, which allows a high level of solar irradiance uniformity on the *PV* cells [14]. This difference, together with their lower cost and lower maintenance [15], allows linear Fresnel reflectors to improve the overall efficiency of *CPV* systems. In addition, several studies have concluded that *CPV* systems are effective technologies for increasing power output and reducing investment cost [16–18]. *HCPV* systems characterised by a high geometric concentration ratio always have a high cost [19]. However, an *LCPV* system with a low geometric concentration ratio will have a low cost [19], meaning it is more suitable for concentrating solar *PV* power production [20,21]. A linear Fresnel reflector (*LFR*) collects sunlight using rows of mirrors to reflect the Sun's rays onto a linear receiver at the top. These mirrors are flat, long, and narrow. Due to the large dimensions of large-scale *LFRs*, their design is characterised by the following: (i) the rows of mirrors are parallel to the horizontal plane, and (ii) the receiver is parallel to the horizontal plane. In contrast, small-scale linear Fresnel reflectors (*SSLFRs*) can incorporate some geometric modifications designed to improve their efficiency given that they are smaller in size.

In [22], a parametric study of an *SSLFR* was presented analysing four configurations in which the rows of mirrors and/or the receiver were tilted with respect to the horizontal plane. The results showed a noticeable increase in incident solar irradiance on the receiver when the receiver was tilted with respect to the horizontal plane. The study did not take into account the effects of receiver tilt or the effects of wind speed on useful energy. Furthermore, the analysed *SSLFR* only generated thermal energy.

The effect of mirror rows and/or receiver tilt on the performance of *SSLFRs* was analysed in [23]. The study was conducted in five cities in the Northern Hemisphere. The receiver tilt angle was varied from 0 (°) to the latitude of the location analysed in 10% intervals. The results also showed a noticeable increase in the energy received by the receiver. This was especially true for those locations where the beam component of the solar irradiance was high. However, the effects of receiver tilt on thermal losses and wind speed were not analysed. The *SSLFR* studied only the thermal energy generated. Ref. [24] theoretically demonstrated the optimum receiver tilt angle for the maximum energy received by the receiver. It concluded that the optimum tilt angle is the one that coincides with the location latitude. The study was implemented in five cities in the Northern Hemisphere. The study did not consider thermal losses due to wind speed. The *SSLFR* only considered the thermal energy generated.

An analysis of the effects of wind (speed and direction) on the heat losses from a receiver at a tilt angle to the horizontal plane of an *SSLFR* using a 3*D* computational fluid dynamics model was presented in [25]. The *SSLFR* was used to obtain thermal energy.

In accordance with the studies analysed, the following conclusions were drawn:

(i) Only a few studies in the literature consider the inclination of the receiver. Studies that take this geometrical design into account discuss obtaining thermal energy.

(ii) There are very few studies in the literature that take into account the inclination of the receiver and the thermal losses due to the action of the wind. These systems are used to generate thermal energy. In addition, they usually use a $3D$ computational fluid dynamics model.

(iii) The studies analysed used the $SSLFR$ to generate thermal energy only.

The contributions of this paper can be summarised in the following points:

(i) The tested $SSLFR$ is used in an $LCPV$ system. To our knowledge, there is no study similar to the one proposed in this paper.

(ii) An experimental platform was designed and built for the development of the tests, allowing the receiver to be tilted.

(iii) The multiple tests carried out took into account five wind speed conditions and seven different conditions: six Northern Hemisphere cities and the classical configuration of large-scale $LFRs$. Four evaluation indicators were used, including useful heat gain, thermal efficiency, solar irradiance gain incident on the PV cells, and total useful energy gain.

(iv) An analysis was performed of electrical efficiency as a function of thermal power and ambient temperature.

(v) A comparison was made between a nonconcentration PV system and a low-concentration PV system.

This paper is organised as follows. Section 2 introduces the basic construction aspects of a low-concentration PV system based on a small-scale linear Fresnel reflector. Section 3 presents the experimental platform, the prototype, the electrical subsystem, the thermal subsystem, the measuring instruments, the experimental procedure, and the evaluation indicators. Section 4 sets forth the experimental results for different tilt angles and different wind speeds. Finally, the conclusions are given in Section 5.

2. An Overview of the LCPV System Based on an SSLFR

The $LCPV$ system studied in this paper is based on an $SSLFR$. The characteristics of this $LCPV$ system are described in [14]. The elements comprising the $SSLFR$ are shown in Figure 1a. The system is roughly composed of two main parts: a primary reflector system and a secondary system. In Figure 1a, the secondary system is aligned with a north–south orientation.

Rows of mirrors are used in this type of solar concentrator to redirect the Sun's rays during the day to a secondary system on top of the fixed structure. The movement of the mirror rows is computer-controlled to keep their reflective surface perpendicular to the angle divider between the directions of the Sun and the secondary system [26].

To more easily understand the $SSLFR$, this study was divided into two planes [26,27]: a transversal plane and a longitudinal plane. Therefore, the angle of incidence of solar irradiance is divided into the transversal angle of incidence (θ_t) and the longitudinal angle of incidence (θ_l).

The primary reflector (PR) system (see Figure 1a) is composed of the parallel mirror rows and the tracking system. This design has a central mirror and an equal number of mirrors on either side of it. The PR system was installed on a mobile structure to provide longitudinal movement.

The parameters required for the transversal design of the PR system are shown in Figure 1b and can be defined as follows: f is the height to the receiver, N is the number of mirrors on each side of the central mirror (therefore, the total number of mirrors is $2N + 1$), W_{Mi} is the width of the i-th mirror, β_i is the angle which mirror i forms with the horizontal, L_i is the position of each mirror with respect to the central mirror (in central mirror $i = 0$, $L_0 = 0$, and β_0), d_i is the separation between two consecutive mirrors, and θ_i is the angle between the vertical at the focal point and the line connecting the centre point of each mirror to the focal point. The parameters required for the longitudinal design of the PR

system are shown in Figure 1c and can be defined as follows: β_M is the angle between the mirror axis and the horizontal plane, and L_M is the length of the mirrors.

The secondary (S) system (see Figure 2) is composed of the PV system, the active cooling system, the secondary structure, the isolation material, the protective casing, and the shaft. The shaft of the S system is installed on a fixed structure.

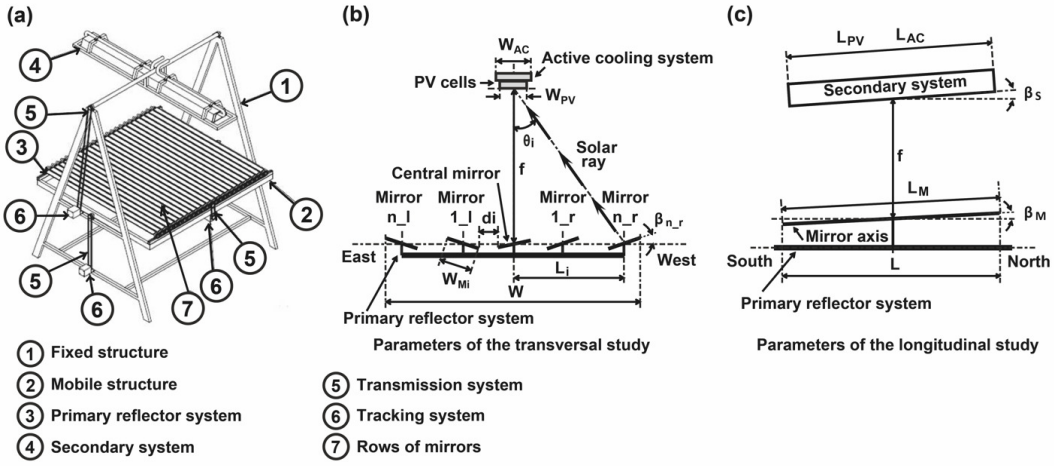

Figure 1. (**a**) Scheme of the SSLFR. (**b**) Parameters of the transversal study. (**c**) Parameters of the longitudinal study

The parameters required for the transversal design of the S system are shown in Figure 1b and can be defined as follows: W_{PV} is the width of the PV cells, and W_{AC} is the width of the active cooling system. The parameters required for the longitudinal design of the S system are shown in Figure 1c and can be defined as follows: β_S is the angle between the PV system and the horizontal plane, L_{PV} is the length of the PV system, and L_{AC} is the length of the active cooling system.

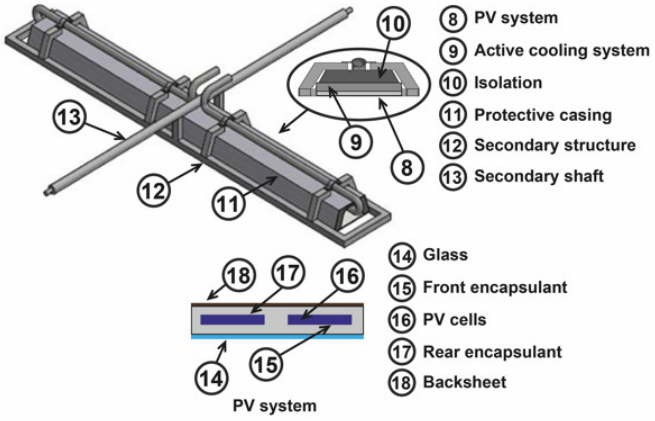

Figure 2. Secondary system.

2.1. Mirrors' Movement

As shown in [26], the motion of each mirror in the primary reflector system is defined by β_i (transversal design). But only the central mirror is controlled, since the rest of the mirrors move at the same angular speed but with a different initial position than the central mirror. The control of the central mirror can be found with the equation

$$\beta_0 = \frac{\theta_t}{2} \quad (1)$$

The initial position of the mirrors on the right side can be found with

$$\beta_i^r = -\beta_0 + \frac{\theta_i}{2};\ 1 \leq i \leq n \quad (2)$$

and the initial position of the mirrors on the left side can be found with

$$\beta_i^l = -\beta_0 - \frac{\theta_i}{2};\ 1 \leq i \leq n \quad (3)$$

2.2. The Longitudinal Tilt Angle of the Secondary System

Several studies have shown the positive effects of *SSLFR* configurations with a longitudinal tilt angle on the primary reflector system and/or the secondary system [23,24,28]. These positive effects are related to the energy absorbed by the secondary system and the surface area required for installation.

A study on the influence of the longitudinal tilt angle on the energy absorbed by the secondary system was presented in [23]. The study was carried out in five cities in the Northern Hemisphere: Almeria (Spain), Rome (Italy), Budapest (Hungary), Berlin (Germany), and Helsinki (Finland). The results obtained were compared with the longitudinal tilt angle used in large-scale *LFRs*, i.e., $\beta_S = 0$ (°). When $\beta_S = \lambda$ (°), the increase in the energy absorbed by the secondary system was maximum [24]. Specifically, there was an increase of 164.14% for Almeria [23]. However, the useful energy was not determined in that study, i.e., thermal losses were not considered, hence the aim of this paper.

3. Experimental Setup

The energy analysis of the influence of the secondary system longitudinal tilt angle focuses on the cooling system, as the primary reflector system and the solar tracking system are considered to be the same and are, therefore, outside the scope of this energy analysis.

An experimental setup was designed and constructed to investigate the consequences of the longitudinal inclination of the secondary system on the efficiency of an *LCPV* system. The experimental data were obtained considering all relevant parameters influencing the overall efficiency of the *SSLFR* secondary system. These parameters are (i) the longitudinal tilt angle of the secondary system, (ii) the dissipated thermal power, (iii) the wind speed, and (iv) the ambient temperature. The width and length of the cooling system and the insulation of the secondary system remained constant throughout the study. Comprehensive experiments were carried out to analyse the behaviour of the secondary system.

3.1. Experimental Platform

As shown in Figure 3, the experimental platform is composed of an *SSLFR* secondary system, an open-loop wind tunnel, an electrical subsystem, a thermal subsystem, the longitudinal inclination of the secondary system, and measuring equipment. The secondary system cooling circuit is connected to the thermal subsystem, and the electrical subsystem simulates the power that the *PV* cells do not transform into electricity.

Figure 4 shows the experimental platform in detail. The experimental analysis was carried out in an open-loop wind tunnel. The air flow was generated by an industrial centrifugal fan. The wind tunnel comprised a flow straightener, a nozzle, a test section, and a diffuser (see Figure 4a). The wind tunnel test section had a diameter of 600 (mm). Figure 4b shows the arrangement of the secondary system inside the wind tunnel test section. Figure 4c shows the longitudinal inclination of the secondary system.

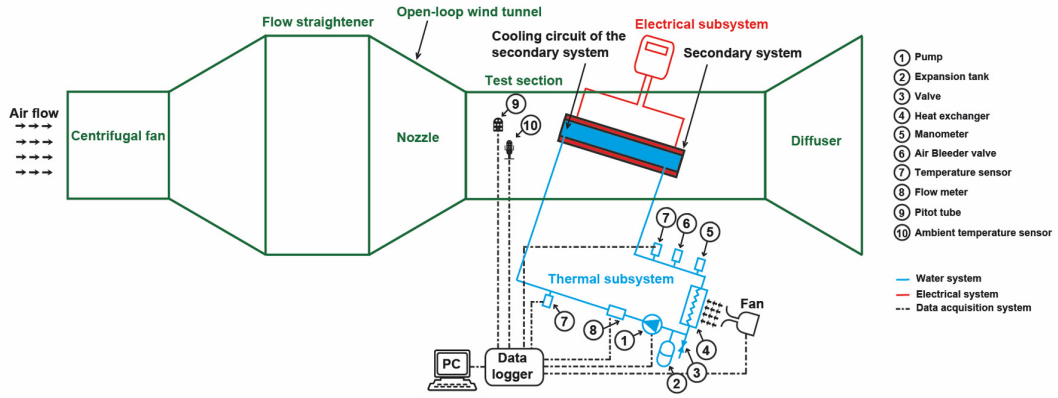

Figure 3. Experimental platform scheme.

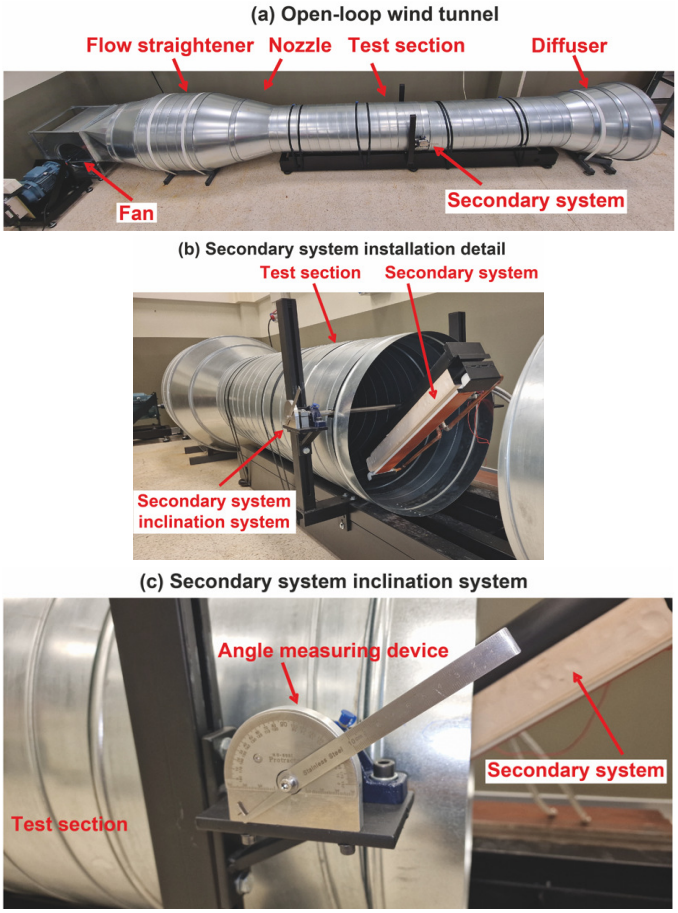

Figure 4. Experimental platform installed.

The experimental platform is located at the Department of Electrical Engineering of the University of Oviedo in Gijón, Spain.

3.2. The Prototype

LCPV systems require uniform illumination of the *PV* cells, otherwise their fill factor and overall electrical efficiency decrease [29] and may even damage the cells [30]. In [14], *SSLFR* parameters were identified which reflect a bad design that can cause nonuniform illumination on *PV* cells. These parameters are as follows: (i) the contribution of shading and blocking phenomena between adjacent mirrors (small d), (ii) high mirror spacing (large d), (iii) the number of mirrors, and (iv) the width of the *PV* system.

Therefore, an $SSLFR$ for $LCPV$ system applications can be considered to be optimally designed when the so-called "optimal design conditions" are met [14]: (i) the flux density over the PV cells is homogeneous; (ii) there is no shading phenomenon between adjacent mirrors; and (iii) there is no blocking phenomenon between adjacent mirrors.

Before defining the measurements of the secondary system being tested, the parameters of the $SSLFR$ need to be calculated. The method proposed in [14] can be used for this purpose. The following parameters were used to apply the methodology proposed in [14]:

(i) The width and length of the prototype are limited by the dimensions of the available wind tunnel. Therefore, a commercial PV cell with a width of 60 (mm) and a length of 30 (mm) was chosen. A total of 21 PV cells were arranged in the PV system. Therefore, the length of the PV system was 658 (mm) ($21 \cdot 30$ (mm)).
(ii) Thermal interface material plays a key role in devices operating at high temperatures, such as photovoltaic concentrator devices or integrated microelectronic devices [31]. Silicone grease [32] was used as the thermal interface material between the PV cells and the cooling system.
(iii) Normally, the height to receiver (f) is taken as 1500 (mm) [14,33,34].
(iv) The choice of the number of mirrors is directly related to the cost of the $SSLFR$ [35]. Nine mirrors were chosen so the cost would not be too high. Therefore, $N = 4$.
(v) Based on the length of the PV system, a mirror length of 658 (mm) was chosen.
(vi) The optical properties of the materials used in the calculations were already used in previous studies [14,36]: mirror reflectivity $\rho = 0.94$ [37], mirror cleanliness $CI_m = 0.96$ [38], glass cleanliness $CI_g = 0.96$ [38], glass transmissivity $\tau_g = 0.92$ [39], encapsulant transmissivity $\tau_e = 0.90$ [40], and PV cell absorptivity $\alpha = 0.90$ [40].
(vii) The optimal design conditions are impossible to meet from sunrise to sunset. Therefore, Ref. [14] defines the so-called "optimum operation interval" (θ_{t_0}). This θ_{t_0} guarantees the homogeneous distribution of solar irradiance without shadows or blocking. Several aspects have to be taken into account when choosing θ_{t_0}, such as the length of the $SSLFR$, the optimal hours of operation, and the total annual solar irradiation effectively reaching the PV cells. As an example, Figure 5 shows three curves related to the choice of θ_{t_0} for the city of Almeria, Spain (latitude 36°50′07″ N, longitude 02°24′08″ W, and elevation 22 (m)), as well as the parameters chosen in this section.

Figure 5a shows the relationship between the number of hours with a guaranteed homogeneous distribution of solar irradiance without shading or blocking and the optimum operation interval. If θ_{t_0} is high, the number of guaranteed hours will also be high. Figure 5b shows the variation of the % of annual irradiation that actually reaches the PV system as a function of θ_{t_0}. If θ_{t_0} is high, the % of annual irradiation will also be high. Figure 5c shows the optimal width of the $SSLFR$ for each value of θ_{t_0}. This curve is convex with a large derivative for larger values of θ_{t_0}. If θ_{t_0} is high, the available roof area will also be high. It should be noted that the available roof area that can accommodate the $SSLFR$ is a critical parameter [41]. Therefore, a balance between the three curves shown in Figure 5 must be found. Based on other studies, θ_{t_0} is considered to be 46 (°) [14,36]. This choice guarantees 74.65% of the unattainable ideal value of 100% annual solar irradiation. In addition, the width of the $SSLFR$ shall be 786.88 (mm), resulting in a nearly square $SSLFR$ area.

Mathematica™ Computer Algebra System software, version 11 was used to determine the optimal parameters. Table 1 shows the optimal design parameters for the primary reflector system. As there are nine mirrors, the central mirror is number 5. As can be seen, there is symmetry in the results, which would be normal for this type of design.

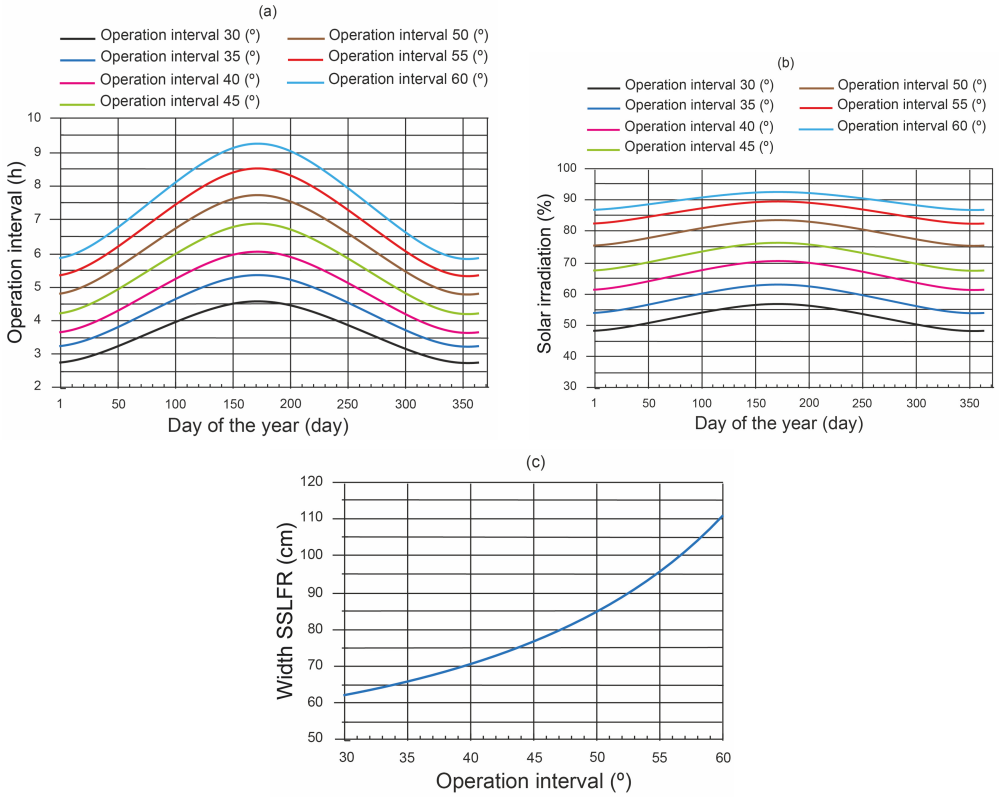

Figure 5. (**a**) Operation interval. (**b**) Solar irradiation. (**c**) Width SSLFR.

Table 1. Optimal design parameters for the primary reflector system.

Mirror	L_i (mm)	W_{Mi} (mm)
1	359.84	67.20
2	267.57	66.93
3	176.65	66.50
4	87.38	65.91
5	0	65.18
6	87.38	65.91
7	176.65	66.50
8	267.57	66.93
9	359.84	67.20

Having defined the primary reflector system and the *PV* system, the dimensions of the prototype can be specified.

A prototype suitable for wind tunnel testing was constructed in order to examine the performance of the secondary system at various inclinations and under real conditions. This prototype is composed of a flat tube (active cooling system) and the corresponding insulation. The cooling medium, which is water in this case, flows through the flat tube. The flat tube is fixed to the secondary system structure by means of u-shaped lateral supports to keep the flat tube in the correct position. The *PV* cells are installed on one side of the flat tube, and the other side is insulated with glass fibre. For this study, the *PV* cells were replaced by an electrical resistor simulating the power that the *PV* cells do not convert into electricity. The prototype is shown in Figure 6. Figure 6a,b show several photographs of the prototype. Figure 6c,d show several schematics of the prototype.

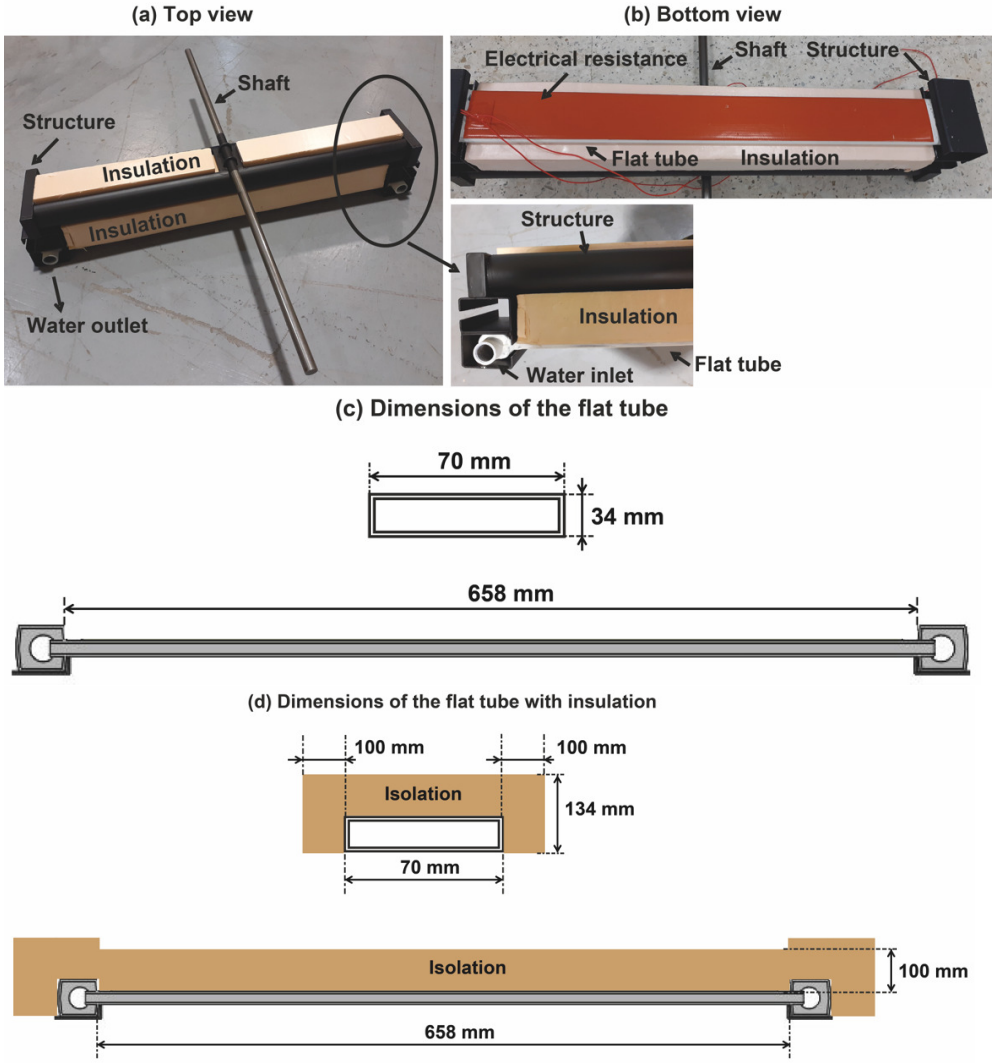

Figure 6. Photographs and schematics of the prototype.

The dimensions of the prototype were chosen so that it could be tested in the available wind tunnel. The prototype is made of the following materials: (i) the flat tube is a carbon steel commercial tube 70.00 (mm) width, 34.00 (mm) height, 658.00 (mm) length, and 2.00 (mm) thick, and the area of the flat tube is 0.046 (m^2); (ii) the insulation comprises a glass wool filling 100 (mm) thick; (iii) the structure is made of a steel square hollow section (mm); (iv) the shaft is a 16 (mm) diameter commercial carbon steel tube; (iv) the electrical resistance has a nominal power of 500 (W) and a nominal voltage of 230 (V).

The secondary system can be rotated on the east–west axis. The secondary system is positioned at a certain longitudinal angle of inclination with respect to the horizontal plane depending on the geographical location of the *SSLFR* and remains in such a position for the duration of the experimental campaign. Therefore, it is essential to have a system (the secondary system inclination system) that meets these requirements. The inclination system is shown in Figure 7. The inclination system includes two bearings (standard bearing type FAG 7205 B.TVP), two bearing supports (standard bearing support type UCP212), and an angle measuring device.

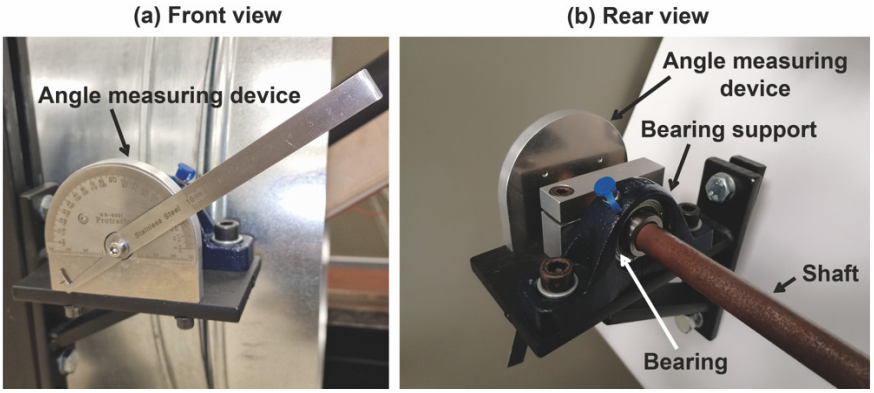

Figure 7. Photographs of the inclination system.

3.3. The Electrical Subsystem

The main objective of the electrical subsystem is to simulate different operating points of the *PV* system from a thermal perspective, i.e., to simulate the thermal power that the *PV* cells do not convert into electricity. The electrical subsystem is composed of a 0–240 (V), 1000 (VA) single-phase variable autotransformer and electrical protections.

3.4. The Thermal Subsystem

In order to examine the performance of the secondary system at various longitudinal inclination angles, a thermal subsystem was constructed. The construction of the thermal subsystem used to dissipate the heat generated in the secondary system was based on ISO 9806: 2017—Test methods for solar thermal collectors [42]. The main objective of the thermal subsystem is to simulate a thermal load that allows the heat generated in the secondary system to be removed. The schematic diagram of the thermal subsystem is shown in Figure 3, and a photograph of this subsystem is shown in Figure 8. The thermal subsystem comprises a pump, an expansion tank, a valve, a heat exchanger, a fan, a pressure gauge, an air bleeder valve, a temperature sensor, and a flow meter. The connection of these devices can be seen in Figure 3. The thermal subsystem comprises a closed circuit with a centrifugal pump taking the water from the outlet of the secondary system where the heating process takes place and pushing it through a heat exchanger, finally returning it to the secondary system inlet. As this is a closed circuit, a heat exchanger (radiator with fan) must be installed to transfer the heat recovered from the secondary system to the environment. Two temperature sensors are also available to record the secondary system inlet and outlet water temperatures. A pressure gauge and a flow meter are present to ensure the circuit pressure and the water flow rate remain constant during the experimental campaign. The fact that the recommended volumetric flow rate for liquid heating solar collectors is between 10 and 50 (L/h) [43] and that thermosyphon-driven liquid-heated solar collectors can reach up to 55 (kg/h) of water mass flow rate [44] was taken into account. The power consumed by the metering equipment, the auxiliary equipment, and centrifugal pump were disregarded as they fall outside the scope of this energy analysis. A constant volumetric water flow rate of 0.5 (L/min) was established for all tests.

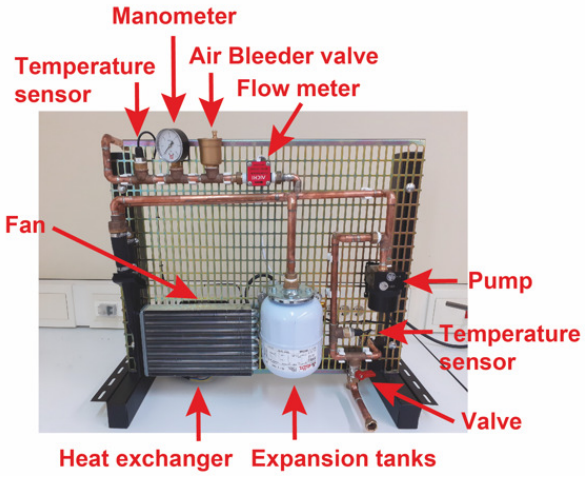

Figure 8. Photograph of the thermal subsystem.

3.5. Measuring Instruments

Experimental measurements included the electrical power, ambient temperature, flow rate, water temperature at the cooling system outlet and inlet, and wind speed. The power absorbed by the electrical resistance was measured with a digital wattmeter type *PX*120 from *MATRIX* [45]. The ambient temperature was measured with a Testo 400 measuring instrument [46] and a T-type thermocouple. The flow rate was measured with a flow sensor type *OF*10*ZAT* from *AICHITOKEI* [47]. Water temperatures were measured by a T-type thermocouple and distributed in the secondary system to measure the temperature at the water inlet/outlet. The wind speed was measured with a Testo 400 measuring instrument [46] and a Pitot tube. These devices were periodically calibrated to ensure traceability of measurements. All instruments were synchronised and all data were captured every 10 (s). Table 2 shows the characteristics of the measuring instruments used in the tests (see Figure 9).

Table 2. Characteristics of the measuring instruments used in the tests.

Parameter	Apparatus	Specifications
Wind speed	Testo 400	Measurement range: 0/40 (m/s) Precision/resolution: 0.5 (%)
	Pitot tube	Measurement range: 0/40 (m/s) Uncertainty: 0.5 (%)
Ambient temperature	Testo 400	Measurement range: −40/150 (°C) Precision/resolution: 0.1 (°C)
	Thermocouple	Measurement range: −40/150 (°C) Uncertainty: 0.1 (°C)
Flow rate	AICHITOKEI	Measurement range: 0.35/5 (L/min) Precision/resolution: 2 (%)
Water temperature	Thermocouple	Measurement range: 0/85 (°C) Uncertainty: 0.0625 (°C)
Electrical power	PX120	Measurement range: 0/1000 (W) Precision/resolution: 1 (%)

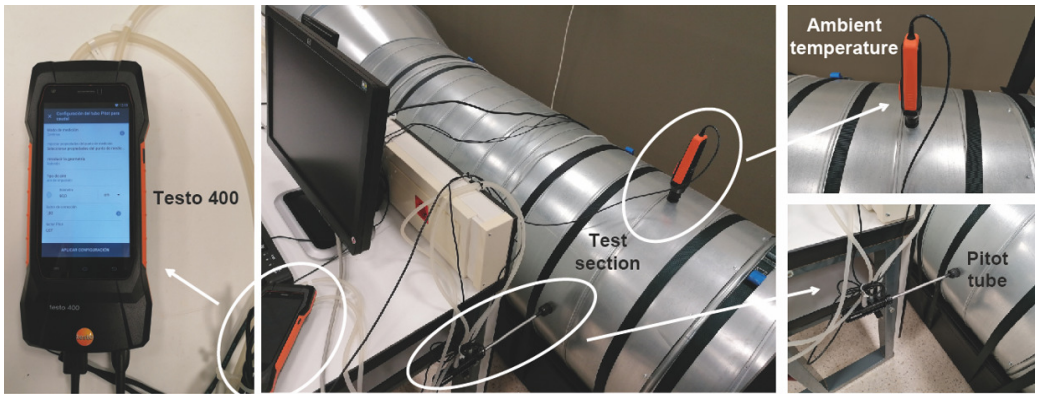

Figure 9. Photographs of the measuring instruments.

Any sources of error in the experiments conducted need to be taken into account to estimate the overall uncertainty associated with the measurements and to then detect inferences from the experimental results. An uncertainty analysis was performed for this reason. Li, et al. [48] identified the different sources of error that can influence the uncertainties of experimental parameters, such as the methodology of the experiments, the calibration of the test rig, the random fluctuation of the instruments used, and the accuracy of observation. The root mean square method was used to determine the measurement uncertainties [49]:

$$e_R = \left[\left(\frac{\partial f}{\partial x_1} e_1 \right)^2 + \left(\frac{\partial f}{\partial x_2} e_2 \right)^2 + \ldots + \left(\frac{\partial f}{\partial x_n} e_n \right)^2 \right]^{\frac{1}{2}} \quad (4)$$

where e_R is the overall uncertainty associated with the measurement, f is the given function of the measurement, and e_1, e_2,..., e_n are the measurement uncertainties of the related measured parameters. Table 3 shows the uncertainties of the parameters used in this study.

Table 3. Computed uncertainty of performance parameter.

Parameter	Parameter Uncertainty (%)
Wind speed	0.7%
Ambient temperature	0.5%
Flow rate	2%
Water temperature	0.5%
Electrical power	1%

Some authors consider experiments to be of high precision for uncertainties when below 2% [50] or 3% [48]. According to the results shown in Table 3, the experiments can be considered as highly accurate.

3.6. Test Conditions

The experimental test campaigns carried out took into account several considerations, such as various longitudinal tilt angles, various wind speeds, various thermal powers, the same electrical efficiency, similar ambient temperatures, the same water flow rate, and the same duration of each test. These considerations are described below.

3.6.1. Longitudinal Tilt Angle

In order to generate a broad image of the energy analysis presented in this study, six cities were selected according to the following criteria:

(i) The cities are located in the Northern Hemisphere. There are several reasons for focusing this study on this hemisphere: (a) Ninety percent of the world's population is concentrated in the Northern Hemisphere [51]. (b) The Northern Hemisphere has

the largest building roof area, which is the ideal location for energy production in cities. In the European Union, there is a total roof area of residential buildings of about 19 billion (m^2) [52].

(ii) There is high beam incident solar irradiance in the chosen city. This is one of the conditions that had to be met for this type of technology to be cost-effective. The SolarGis software [53] uses data from 19 high-precision satellites for its simulations and provides maps with a rigorous, systematic approach of different parts of the world. Figure 10 shows a map of the direct normal solar irradiation all over world.

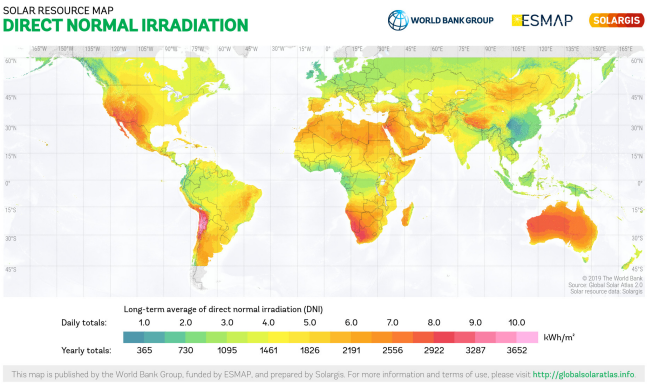

Figure 10. Direct normal irradiation map all over world [53].

(iii) There are different climate zones with quite different latitudes. In [24], they propose the choice of study locations with a difference of about 6 (°) latitude starting at latitudes of 36 (°) up to 60 (°). In our study, locations higher than 40 (°) latitude are not considered due to the value of the incident direct solar irradiance.

Table 4 shows the geographic characteristics of the cities under study.

Table 4. Cities under study.

	Cities	Latitude	Longitude	Altitude
1	Medellin (Colombia)	06°14′38″ N	75°34′04″ W	1469 (m)
2	Bangkok (Thailand)	13°45′14″ N	100°29′34″ E	9 (m)
3	Morelia (Mexico)	19°42′10″ N	101°11′24″ W	1921 (m)
4	Karachi (Pakistan)	24°52′01″ N	67°01′51″ E	14 (m)
5	Cairo (Egypt)	30°29′24″ N	31°14′38″ W	41 (m)
6	Almeria (Spain)	36°50′07″ N	02°24′08″ W	22 (m)

Figure 11 shows some environmental conditions at the locations under study. This figure shows the daily mean temperature and daily normal irradiance with solar tracking for the month of June. The highest solar irradiance values occur in this month. The values shown in Figure 11 are obtained from the PVGIS database [54].

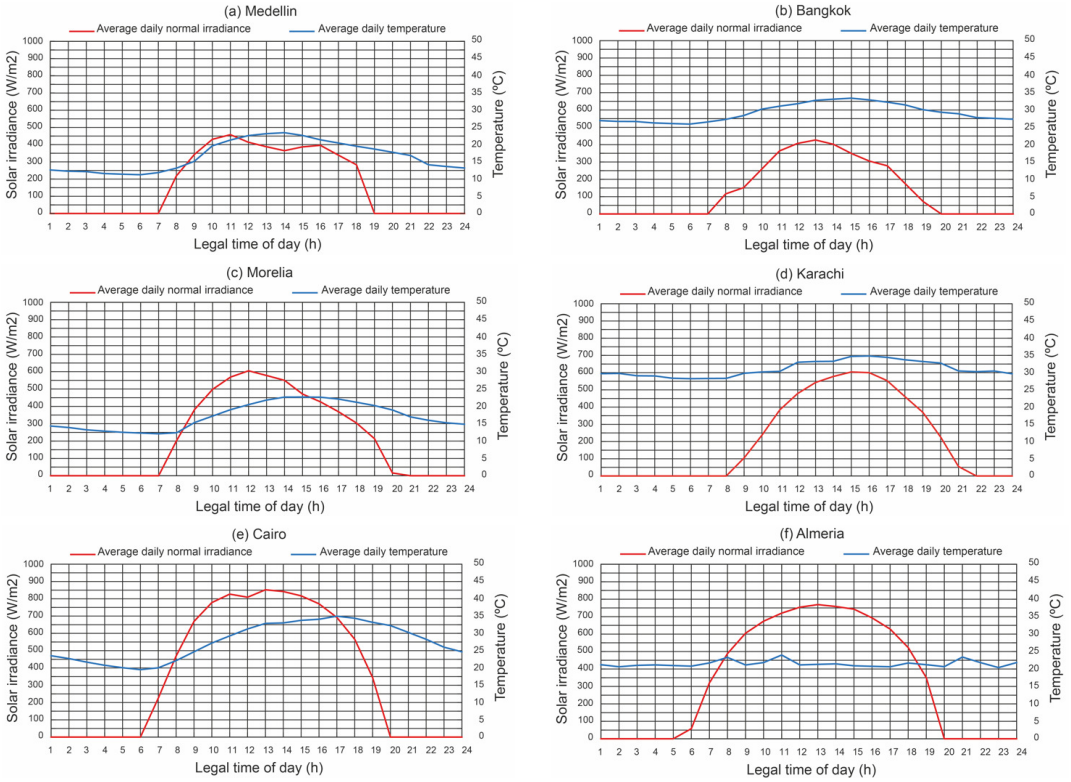

Figure 11. Environmental conditions.

(iv) The optimal longitudinal tilt angle of the secondary system demonstrated in [24] is used to define the longitudinal tilt angle at each chosen location. This angle coincides with the latitude of the location.

3.6.2. Wind Speed

A wind tunnel was used to provide different wind speeds. The wind speeds chosen depend on the characteristics of the wind tunnel. Five different wind speeds (around 0 (m/s), 1.05 (m/s), 2.55 (m/s), 4.99 (m/s), and 10.03 (m/s)) were investigated.

3.6.3. Water Flow Rate

During the tests, the water flow rate remained around 0.5 (L/min) to simulate thermosyphon operation.

3.6.4. Ambient Temperature

Ambient temperature is a parameter that influences the results. The ambient temperature at the start of each test ranged from 19.00 (°C) to 20.70 (°C).

3.6.5. Duration of Each Test

Each test used a longitudinal tilt angle, dissipated thermal power, and five wind speeds. The duration of each test was five hours. A total of seventy hours were spent on the research. Each test was carried out on a different day.

3.6.6. Thermal Power

Depending on the PV cell mode of operation, a significant part of the absorbed solar irradiance may not be converted into electricity and is, therefore, completely dissipated as heat. This internal heat source can be expressed according to the following equation [55]:

$$Q_{th} = I_t \cdot A_{PV} \cdot (1 - \eta_e) \quad (5)$$

where Q_{th} is the internal heat source (W), I_t is the total absorbed solar irradiance for the PV system (W/m^2), A_{PV} is the total area of the PV system (m^2), and η_e is the electrical efficiency of the PV system.

Part of the heat Q_{th} is transferred by conduction to the wall of the flat tube, according to Fourier's law of conduction [56]:

$$Q_{cond} = \frac{k \cdot A_{AC} \cdot (T_{PV} - T_{AC})}{\delta_{AC}} \quad (6)$$

where k is the thermal conductivity of the flat tube (W/m°K), A_{AC} is the area of the flat tube (m^2), T_{PV} is the temperature of the PV cells (°K), T_{AC} is the temperature of the flat tube (°K), and δ_{AC} is the wall thickness of the flat tube (m). In this study, $k = 50$ (W/m°K).

The heat is transferred by convection to the working fluid through the wall of the flat tube, according to Newton's Law of Cooling [56]:

$$Q_{conv} = h_i \cdot A_{AC} \cdot (T_{AC} - T_w) \quad (7)$$

where h_i is the heat transfer coefficient of the wall of the flat tube (W/m^2°K), A_{AC} is the area of the flat tube (m^2), T_{AC} is the surface temperature of the wall of the of the flat tube, and T_w is the working fluid temperature. h_i can be determined using the following equation [57]:

$$h_i = \frac{k_w}{D_h} \cdot 0.23 \cdot R_{ew}^{0.8} \cdot P_{rw}^{0.4} \quad (8)$$

where k_w is the thermal conductivity of the working fluid (W/m°K), D_h is the hydraulic diameter of the flat tube (m), R_{ew} is the Reynolds number of the working fluid, and P_{rw} is the Prandtl number of the working fluid.

Part of the heat Q_{th} is transferred by convection (Q_{convPV}) and radiation (Q_{radPV}) to the environment. According to the Stefan–Boltzmann law [56],

$$Q_{radPV} = \sigma \cdot \varepsilon_{PV} \cdot A_{PV} \cdot \left(T_{PV}^4 - T_{amb}^4\right) \quad (9)$$

where σ is the Stefan–Boltzmann constant which is equal to $5.67 \cdot 10^{-8}$ (W/m^{2}K^4), ε_{PV} is the emittance of the PV system, A_{PV} is the total area of the PV system (m^2), T_{PV} is the temperature of the PV cells (°K), and T_{amb} is the ambient temperature (°K). In this study, $\varepsilon_{PV} = 0.9$ [57]. According to Newton's Law of Cooling [56],

$$Q_{convPV} = h_{PV} \cdot A_{PV} \cdot (T_{PV} - T_{amb}) \quad (10)$$

where h_{PV} is the heat transfer coefficient of the PV system (W/m^2°K), A_{PV} is the total area of the PV system (m^2), T_{PV} is the temperature of the PV cells (°K), and T_{amb} is the ambient temperature (°K). The heat losses of the flat tube are considered negligible due to the insulation consisting of a glass wool filling 100 (mm) thick. Figure 12 shows a simplified heat transfer scheme.

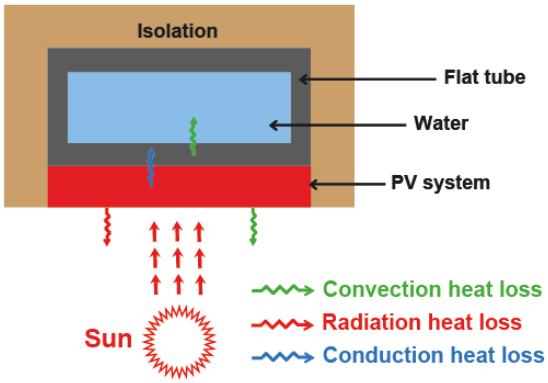

Figure 12. Simplified heat transfer scheme.

3.6.7. Electrical Efficiency

The electrical efficiency of a photovoltaic cell depends on its operating temperature [58]:

$$\eta_e = \eta_{ref} \cdot \left[1 - \beta_{ref} \cdot \left(T_{PV} - T_{ref}\right)\right] \quad (11)$$

where η_e is the electrical efficiency of the PV system at the operating temperature (dimensionless), η_{ref} is the electrical efficiency of the PV system at 25 (°C) and a solar irradiance of 1000 (W/m^2) (dimensionless), β_{ref} is the temperature coefficient at 25 (°C) (1/°C), T_{PV} is the PV cell temperature (°C), and T_{ref} is the reference temperature of 25 (°C). The parameters η_{ref} and β_{ref} are provided by the PV cell manufacturer, 0.209 and 0.0035 (°C^{-1}), respectively.

3.6.8. Thermal Energy Chosen for the Test

The thermal power not converted into electricity by the PV system (see Equation (5)) depends on the solar irradiance and electrical efficiency of the PV system, which in turn depend on the ambient temperature and solar irradiance. These parameters depend on the location, day, and time chosen (see Figure 11). Therefore, the choice of thermal energy not converted into electricity by the PV system depends on multiple parameters. The thermal power not converted into electricity by the PV system chosen was 300 and 400 (W). These values were chosen for the following reasons:

(i) The concentration factor of the $LCPV$ system is 10.41. To determine this value, the parameters of the primary reflector system shown in Table 1 and the dimensions of the prototype were used. With the incident solar irradiance at the Cairo and Almeria locations, a thermal power not converted into electricity by the PV system of approximately 300 (W) is obtained.
(ii) The choice of 300 (W) allows the Medellin, Bangkok, Morelia, and Karachi locations to increase the $LCPV$ concentration factor in future studies.
(iii) The choice of 400 (W) allows all locations under study to be able to increase the $LCPV$ concentration factor in future studies.

Figures 13 and 14 show the results of the average water temperature in the flat tube obtained in the tests, the ambient temperature at which the test was performed, and the average temperature of the PV system obtained using Equations (6)–(10). From the test, T_w and Q_{conv} are obtained, and by means of Equations (8) and (7), T_{AC} is obtained. Once T_{AC} is known, by means of Equation (6), T_{PV} is obtained. On the other hand, once T_{PV} is known, Q_{radPV} can be determined by Equation (9). Q_{convPV} can be obtained by subtracting the losses Q_{cond} and Q_{radPV} from Q_{th}.

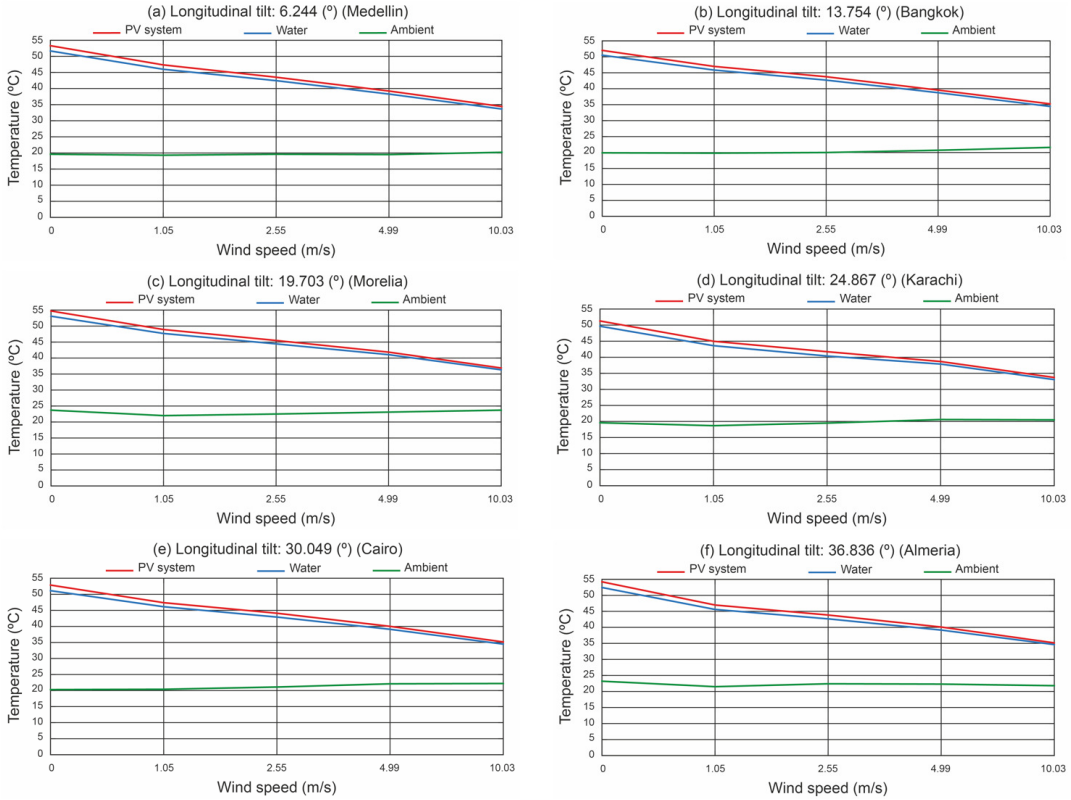

Figure 13. Temperatures for power not converted into electricity by the PV cells of 300 (W).

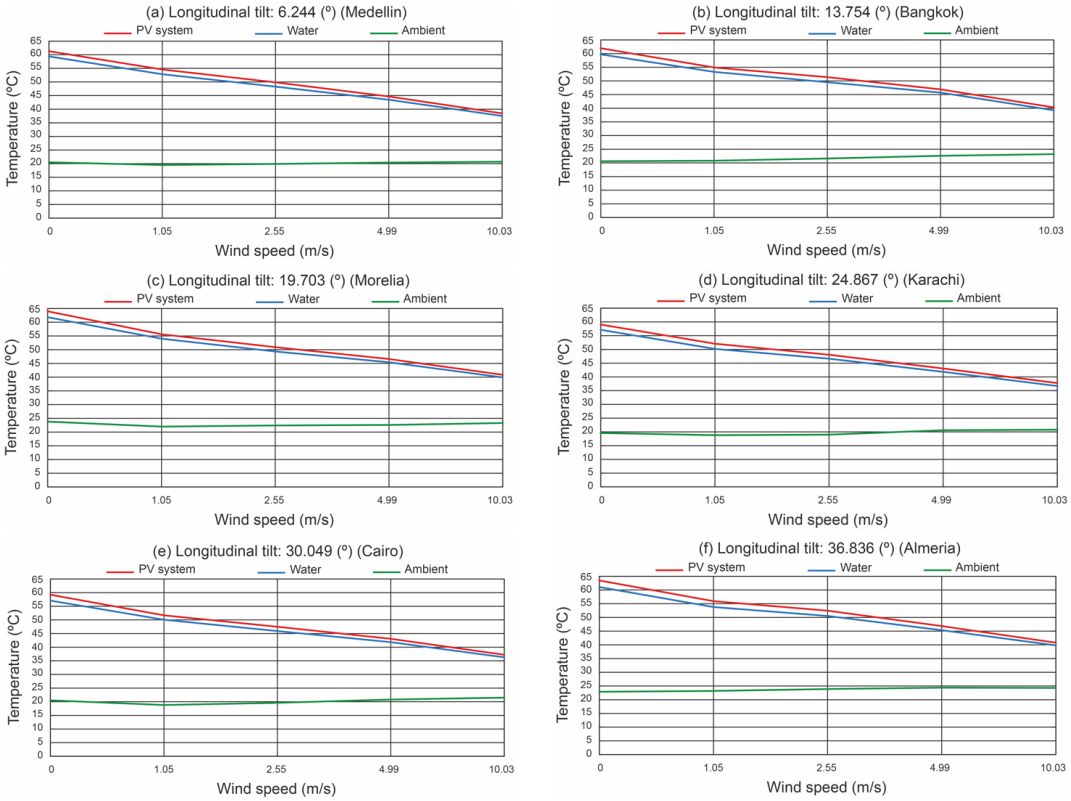

Figure 14. Temperatures for power not converted into electricity by the PV cells of 400 (W).

3.7. Experimental Procedure

Different environmental conditions, such as wind speed and ambient temperature, were recorded. In addition, the thermal power that the photovoltaic cells did not convert into electricity was also recorded. Several longitudinal tilt angles of the secondary system were used in the study. The experimental procedure was carried out according to the following steps:

(i) The water was circulated through the cooling system by the pump to simulate thermosyphon operation. The flow meter registered the water flow rate, and a valve was used to keep it constant.
(ii) The electrical resistance simulated the energy that the photovoltaic cells do not convert into electricity. An autotransformer was used to ensure that the thermal power remained constant throughout the test.
(iii) The test started with a wind speed of 0 (m/s), and every hour the wind speed was increased up to 10.03 (m/s).
(iv) The following parameters were measured during the test: the power absorbed by the electrical resistance, the ambient temperature, the water flow rate, the temperature at the water inlet/outlet, and the wind speed.

3.8. Assessment Parameters

Two *SSLFR* configurations were compared for this paper: a base configuration (classical configuration of large-scale *LFRs*) and a longitudinal tilt configuration. The base configuration (C_B) is characterised by $\beta_M = 0$ (°) and $\beta_S = 0$ (°), and the longitudinal tilt configuration (C_S) is characterised by [24] $\beta_M = \lambda/2$ (°) and $\beta_S = \lambda$ (°).

3.8.1. Useful Heat Gain

As mentioned above, the part of the absorbed solar irradiance that is not converted into electricity by the *PV* system is completely dissipated as heat (Q_{th}). But not all of this heat is used to increase the performance of the system, as there are heat losses.

The useful heat, Q_u, can be written as follows [59]:

$$Q_u = m \cdot C_p \cdot (T_{out} - T_{in}) \tag{12}$$

where m is the fluid mass flow rate (kg/s), Cp is the heat capacity of the water (J/kg °C) evaluated at the average temperature, T_{in} is the temperature of the inlet fluid to the secondary system (°C), and T_{out} is the temperature of the outlet fluid to the secondary system (°C).

This study evaluates the useful heat gain (UHG) due to the longitudinal tilt configuration (C_S) of the secondary system with respect to the base configuration (C_B). To do so, the difference between the useful heat with the configuration studied and the base configuration must be calculated. These values are % useful heat loss, as concerns the base configuration, i.e.,

$$UHG = \frac{Q_{uC_S} - Q_{uC_B}}{Q_{uC_B}} \cdot 100 \tag{13}$$

3.8.2. Thermal Efficiency

The influence of the longitudinal tilt angle of the secondary system is determined by the thermal efficiency (η_{th}) of the cooling system defined as the ratio between the useful heat and the power not converted into electricity by the photovoltaic cells.

$$\eta_{th} = \frac{Q_u}{Q_{th}} \tag{14}$$

where Q_u is the useful heat (W) and Q_{th} is the power not converted into electricity by the *PV* system (W).

3.8.3. Solar Irradiation Gain Incident on the PV Cells

The beam solar irradiation gain incident on the PV cells can be determined according to the following equation:

$$H_bG = \frac{H_{bC_S} - H_{bC_B}}{H_{bC_B}} \cdot 100 \quad (15)$$

where H_{bC_S} is the beam solar irradiation incident on the PV cells in a longitudinal tilt configuration (kWh), and H_{bC_B} is the beam solar irradiation incident on the PV cells in a base configuration (kWh). If H_bG is positive, a longitudinal tilt configuration performs better; however, a base configuration performs better if H_bG is negative.

3.8.4. Total Useful Energy Gain

In a CPV system, the total useful energy is the sum of electrical energy and thermal energy. To compare the two configurations, the total useful energy gain will be used:

$$EG = \frac{E_{C_S} - E_{C_B}}{E_{C_B}} \cdot 100 \quad (16)$$

where E_{C_S} is the total useful energy in a longitudinal tilt configuration (kWh), and E_{C_B} is the total useful energy in a base configuration (kWh).

4. Experimental Results and Discussion

The aim of this section is to estimate the effect of a longitudinal tilt angle for the secondary system of a low-concentration PV system based on a small-scale linear Fresnel reflector and the wind speed on the proposed evaluation indicators: useful heat gain, thermal efficiency, solar irradiation gain incident on the PV cells, and total useful energy gain. Two configurations were analysed for this purpose: a base configuration and a longitudinal tilt configuration. The base configuration (C_B) is the classical configuration of large-scale $LFRs$ and is characterised by $\beta_M = 0$ (°) and $\beta_S = 0$ (°). The longitudinal tilt configuration (C_S) is characterised by the optimal longitudinal tilt angles [24] $\beta_M = \lambda/2$ (°) and $\beta_S = \lambda$ (°). Experimental tests were carried out for various geographical locations and compared with the longitudinal tilt angle used in large-scale $LFRs$.

The available flat roof surface of the building was considered to be the same for all studies carried out. Specifically, the dimensions of the flat roof were a width of 78.68 (mm) and a length of 658 (mm). The electrical efficiency of the PV cells was also assumed to be the same for both configurations. In fact, 0.2 was assumed for the two. Moreover, the operating temperature of the PV cells was assumed to be the same in both configurations for the same wind speed.

The useful heat of the secondary system was determined for various longitudinal tilt angles, various powers that the PV cells did not convert into electricity, and various wind speeds. Section 3 shows the dimensions and materials of the prototype under testing. The conditions of the experimental tests conducted were as follows: (i) a range of longitudinal tilt angles from 0 (°) to 36.86 (°) at intervals of approximately 6 (°); (ii) a wind speed range of 0 (m/s) to 10.03 (m/s); (iii) an initial ambient temperature range of 19.00 (°C) to 20.70 (°C); (iv) two situations of unconverted electricity power from the PV cells of 300 (W) and 400 (W); and (v) a water flow rate through the cooling system of 0.5 (L/min). The thermal performance of the prototype was examined by monitoring the thermal behaviour while varying the wind speed and the longitudinal tilt angle of the secondary system.

Mathematica™ Computer Algebra System software was used to determine the irradiance incident on the PV system. This software has been used extensively in similar studies [14]. In order to be able to analyse how the experimental results affect the $SSLFR$ configuration, the beam solar irradiance incident on the PV system must be determined. Thus, the beam solar irradiance on the horizontal surface of the site under study and, therefore, the specific meteorological conditions must be taken into account. The method proposed by [60] can be used to determine the particular meteorological conditions at a

given location. This method uses the $PVGIS$ [54] database to obtain the monthly average beam solar irradiance over horizontal surfaces. The equations used for the calculation of the incident solar irradiation on the PV system are presented in [14]. Table 5 shows the beam solar irradiation incident (H_b) on the PV cells for each configuration and city studied. This table also shows the beam solar irradiation incident gain (H_bG) with respect to the base configuration (H_{bC_B}).

Table 5. Beam solar irradiation incident on PV cells.

	Cities	H_{bC_B} (kWh)	H_{bC_S} (kWh)	H_bG (%)
1	Medellin (Colombia)	235.43	248.10	5.38
2	Bangkok (Thailand)	310.30	354.67	14.30
3	Morelia (Mexico)	452.55	532.21	17.60
4	Karachi (Pakistan)	418.83	528.83	26.26
5	Cairo (Egypt)	472.14	648.10	37.27
6	Almeria (Spain)	443.08	680.19	53.51

As can be seen in Table 5, the effect of the longitudinal tilt of the secondary system is positive with respect to the incident solar irradiation on the PV cells.

4.1. Effect of the Longitudinal Tilt Angle of the Secondary System on Useful Heat

Figure 15 shows the useful heat for the longitudinal tilts under study and the 400 (W) power not converted into electricity by the PV cells.

Figure 15 suggests the following conclusions as concerns the useful heat:

(i) Useful heat obviously decreases as the wind speed increases. This effect is more noticeable as the longitudinal tilt angle increases.

(ii) When the wind speed is 10.03 (m/s), the useful heat gain (UHG) of the longitudinal tilt configuration is between −21.30% (Medellin) and −33.91% (Almeria) with respect to the base configuration. For this wind speed, there is a noticeable difference in UHG between the lower latitude and higher latitude locations.

(iii) If the wind speed is 4.99 (m/s), the UHG is between −17.27% (Medellin) and −18.77% (Almeria). The difference in useful heat gain between the most extreme locations decreases considerably with this wind speed.

(iv) When the wind speed is 2.55 (m/s), the useful heat gain in the longitudinal tilt configuration is still lower than in the base configuration. UHG is approximately −8%. In this case, the difference in useful heat gain between the most extreme locations is negligible. The same is true for a wind speed of 1.05 (m/s).

(v) When the wind speed is 0 (m/s), the useful heat gain in the longitudinal tilt configuration is similar to that of the base configuration.

(vi) It can be concluded that the presence of wind is detrimental to the longitudinal tilt configuration at all locations as concerns the useful heat. However, it is important to note that this type of technology also generates electricity. Furthermore, according to Table 5, the longitudinal tilt configuration performs better as concerns incident solar irradiation on the PV system. This will be assessed in the study below.

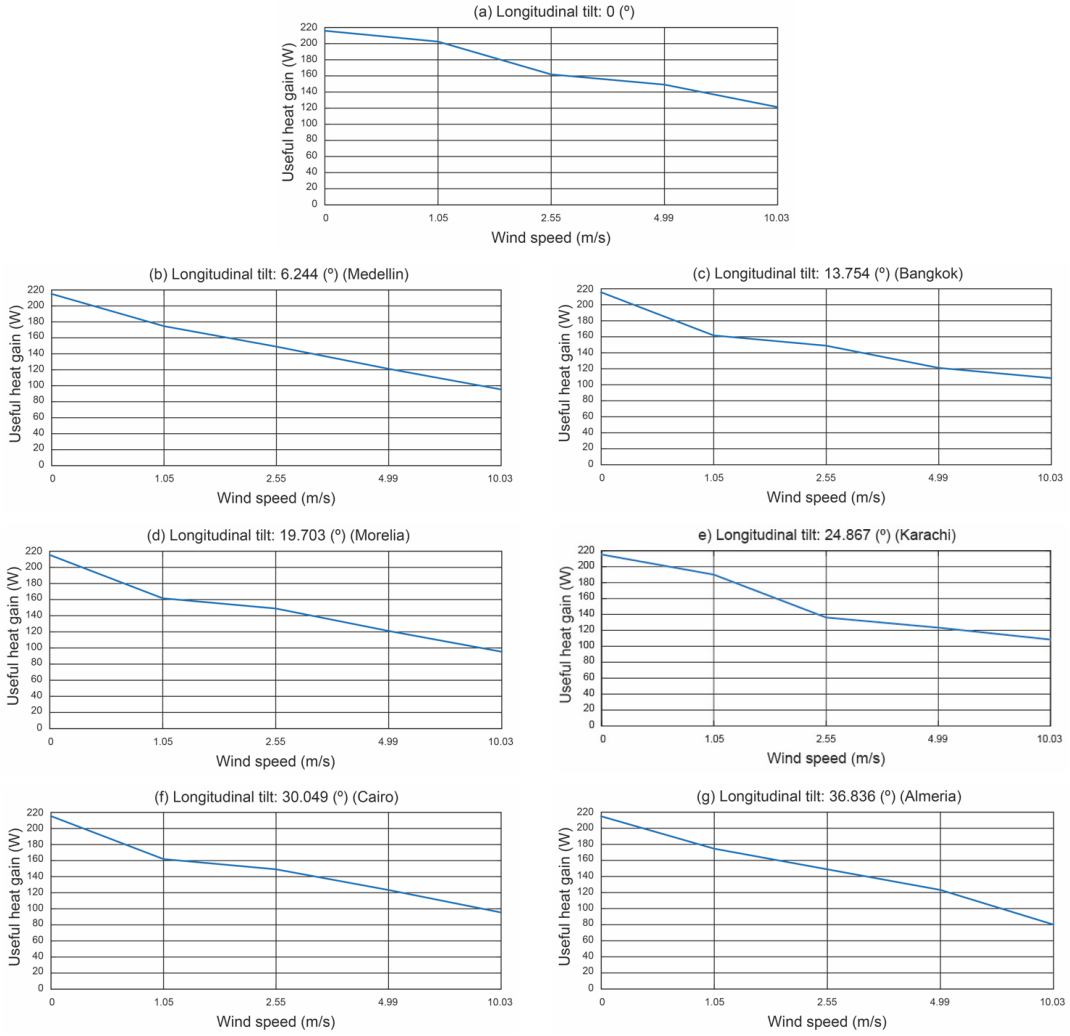

Figure 15. Useful heat for power not converted into electricity by the PV cells of 400 (W).

Figure 16 shows the useful heat for the longitudinal tilts under study and the power not converted into electricity by the photovoltaic cells of 300 (W). Figure 13 shows similar trends in useful heat as Figure 15. The trends for useful heat gain are also true.

4.2. Effect of the Longitudinal Tilt Angle of the Secondary System on Thermal Efficiency

Figure 17 shows the thermal efficiency for the longitudinal tilts under study and the power not converted into electricity by the photovoltaic cells of 400 (W).

Figure 17 suggests the following conclusions:

(i) The trend obtained with useful heat (see Figure 15) is also obviously true for thermal efficiency.

(ii) The thermal efficiency is always below 0.6. As wind speed increases, this value decreases. This effect is more pronounced as the longitudinal tilt angle increases.

(iii) When the wind speed is 1.05 (m/s), the thermal efficiency ranges between 0.5 and 0.4. For wind speeds of 2.55 (m/s), it ranges between 0.4 and 0.3. For wind speeds of 4.99 (m/s) and 10.03 (m/s), the thermal efficiency is between 0.3 and 0.2. This is valid for all locations. The lowest thermal efficiency is obtained in Almeria (location with the highest latitude).

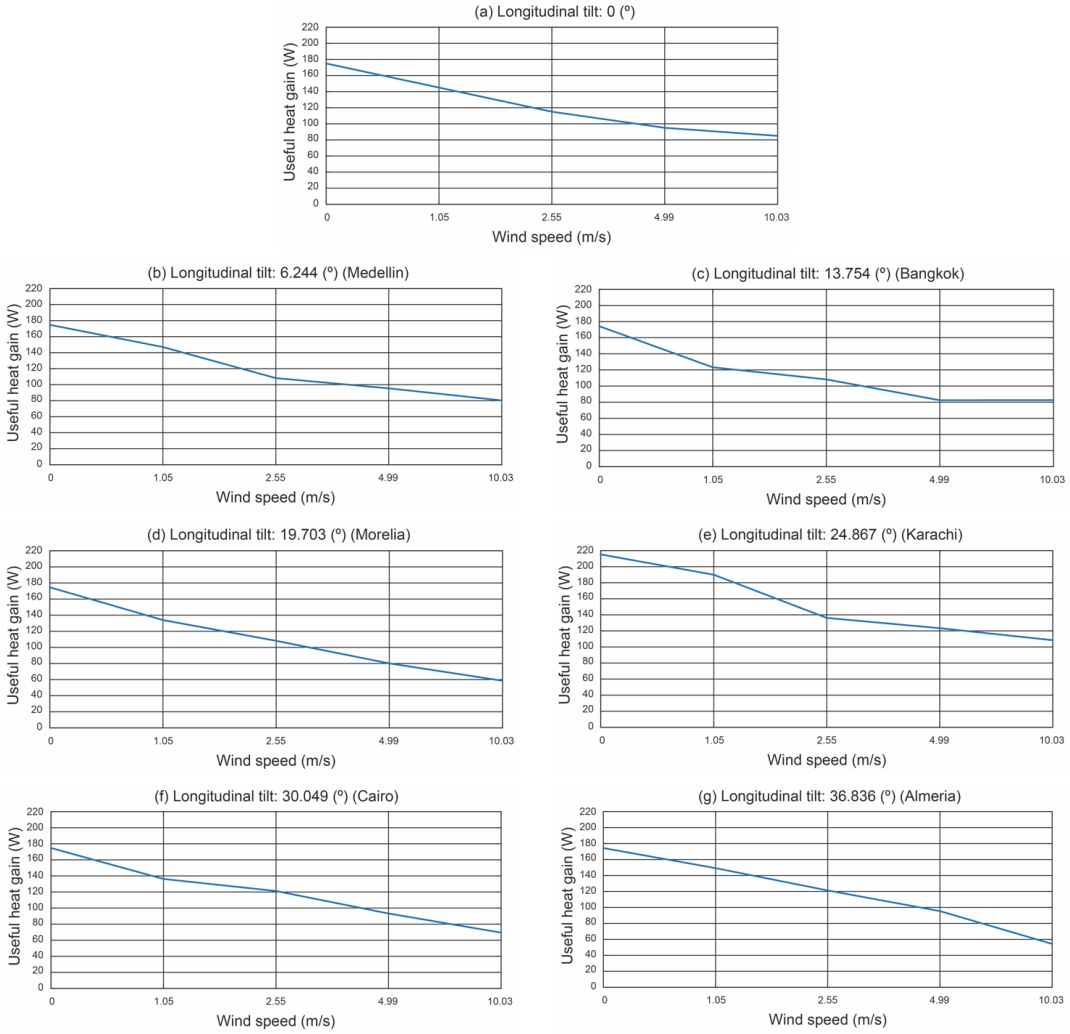

Figure 16. Useful heat for power not converted into electricity by the PV cells of 300 (W).

Figure 18 shows the thermal efficiency for the longitudinal tilts under study and power not converted into electricity by the photovoltaic cells of 300 (W). The conclusions drawn in Figure 17 are applicable to Figure 18.

4.3. Effect of the Longitudinal Tilt Angle of the Secondary System on Total Useful Energy Gain

The total useful energy in the configurations studied is the sum of the electrical energy generated and the useful thermal energy. As shown in Table 5, the incident solar irradiation on the *PV* system increases with increasing longitudinal tilt angle. This is an important factor in this study. Figure 19 shows the total useful energy gain for the two configurations as a function of two wind speeds. The longitudinal tilt configuration shows the best total useful energy gain in the absence of wind. The lowest latitude location (Medellín) has the smallest increase. On the other hand, for higher latitudes, the total useful energy gain reflects values up to 53%. The longitudinal tilt configuration still performs the best when the wind speed is 10.03 (m/s), except at the lowest latitude location. The total useful energy gain at this wind speed decreases to 25% for the highest latitude location (Almeria). Therefore, it can be concluded that secondary system designs with longitudinal tilt angles perform well at locations with latitudes above 10 (°). These results are quite good if the latitude is higher than 24 (°) and lower than 37 (°).

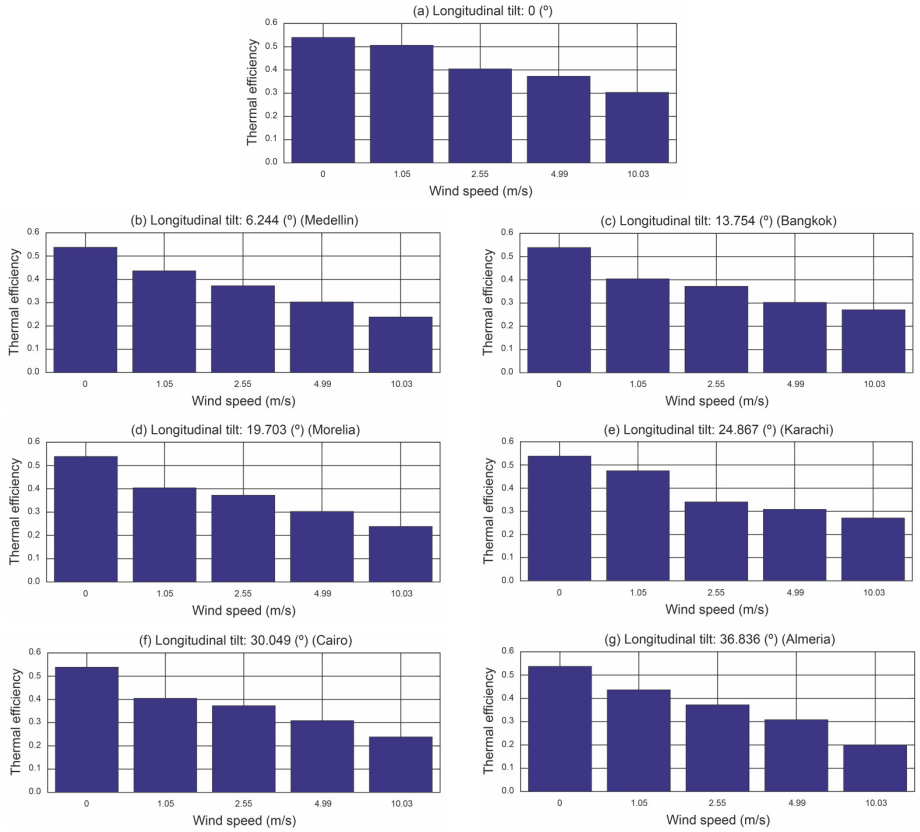

Figure 17. Thermal efficiency for power not converted into electricity by the PV cells of 400 (W).

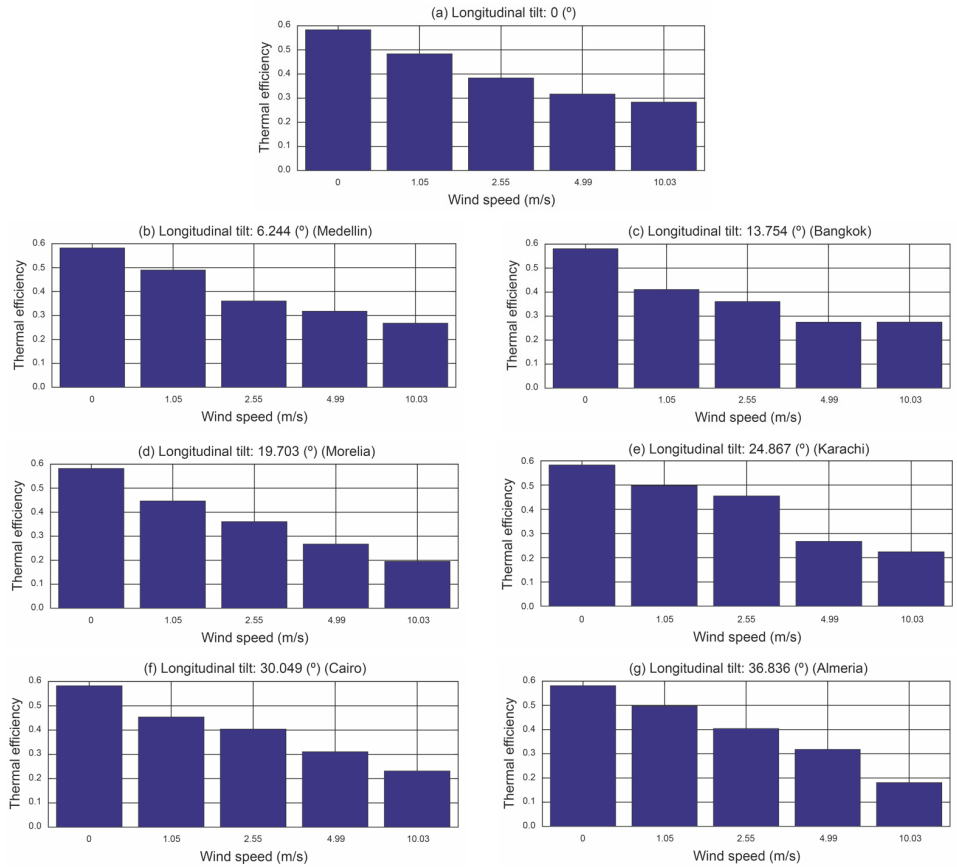

Figure 18. Thermal efficiency for power not converted into electricity by the PV cells of 300 (W).

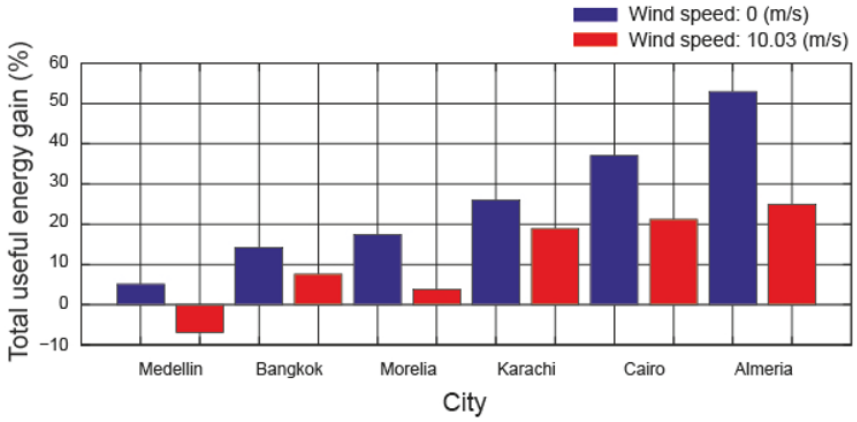

Figure 19. Total useful energy gain.

4.4. Effect of Thermal Power on the Electrical Efficiency of the PV System

As the solar irradiance incident on the *PV* system increases, the nonconverted electricity output increases. Figure 20 shows the electrical efficiency for 300 and 400 (W) with the results obtained in the tests.

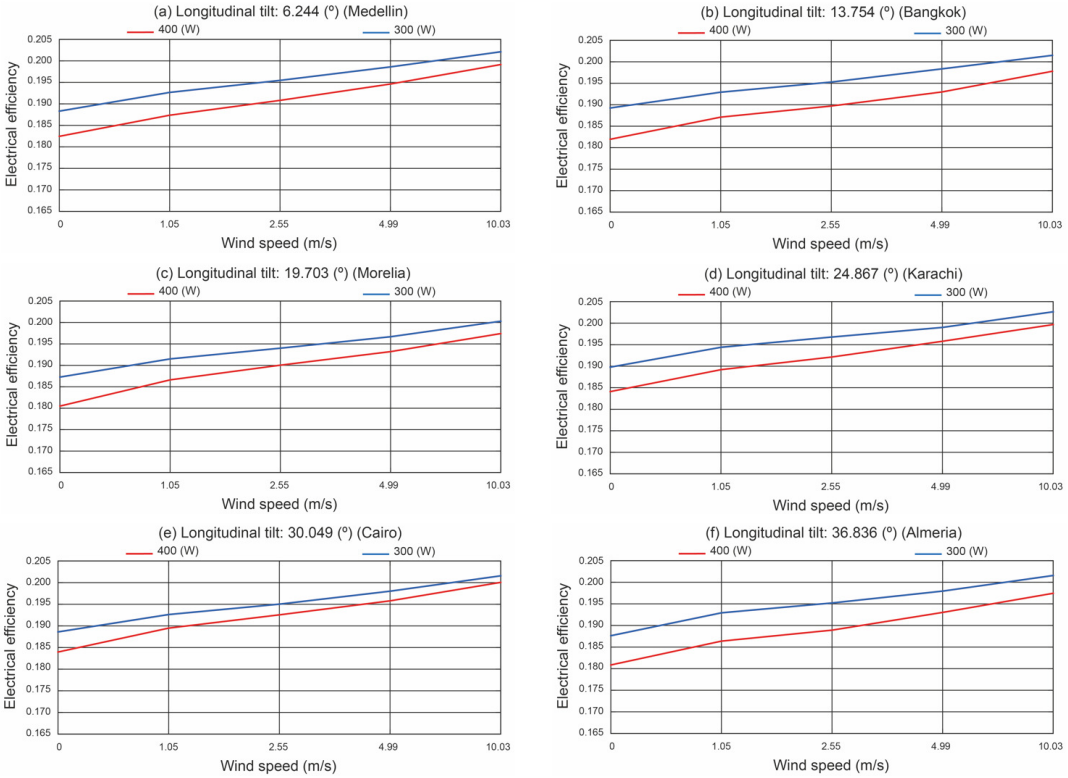

Figure 20. Electrical efficiency for 300 and 400 (W) thermal power.

Figure 20 suggests the following conclusions as concerns the electrical efficiency:

(i) Electrical efficiency increases as the wind speed increases and as the operating temperature of the *PV* cell decreases.
(ii) Electrical efficiency decreases as the thermal power of the *PV* system increases and as the incident solar irradiance on the *PV* system increases.
(iii) The difference in electrical efficiency for 300 and 400 (W) decreases with increasing wind speed as the operating temperature of the *PV* cells decreases.

4.5. Effect of Ambient Temperature on the Electrical Efficiency of the PV System

In this section, the electrical efficiency was determined numerically for 30 and 40 (°C) ambient temperature. According to Figure 11, the ambient temperature of the studied locations does not exceed 40 (°C). It can be considered that the losses Q_{convPV} and Q_{radPV} remain constant if the solar irradiance remains constant. According to Mattei et al. [61], if the solar irradiance remains constant, the temperature of the PV system increases in the same proportion as the ambient temperature. Figures 21 and 22 show the electrical efficiency for ambient temperatures of 30 and 40 (°C), respectively.

Figures 21 and 22 suggest the following conclusions as concerns the electrical efficiency:

(i) The electrical efficiency obviously decreases as the ambient temperature increases, since the operating temperature of the PV cell increases.
(ii) The increase in wind speed dampens the decrease in electrical efficiency, but not enough to offset the increase in ambient temperature.
(iii) Therefore, increasing the ambient temperature decreases the electrical efficiency but increases the thermal efficiency of the system by decreasing the thermal jump between the ambient temperature and the heat source.

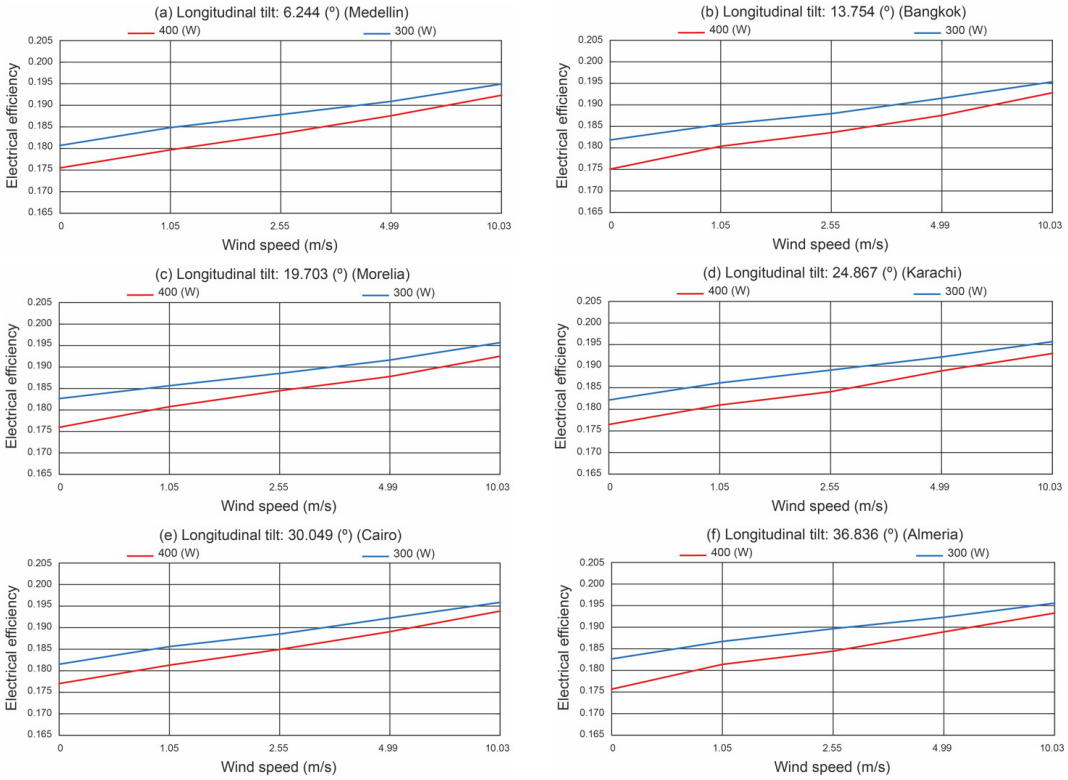

Figure 21. Electrical efficiency for an ambient temperature of 30 (°).

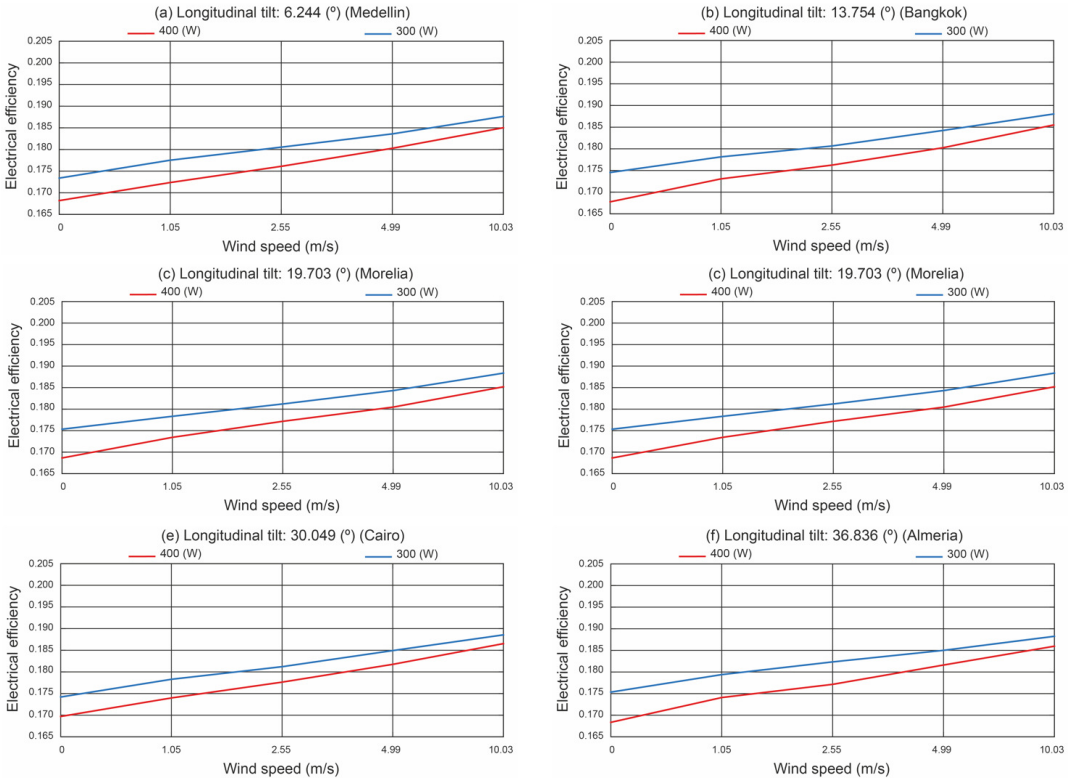

Figure 22. Electrical efficiency for an ambient temperature of 40 (°).

4.6. Efficiency Comparison between Concentrating and Nonconcentrating PV Systems

In this section, the results obtained above will be applied to compare the *NCPV* system and the *CPV* system. The following assumptions were considered in order to compare the two systems:

(i) The available roof area of the building was considered to be the same for both technologies. Specifically, the flat roof has a width of 786.88 (mm) and a length of 658 (mm).
(ii) According to Figures 20–22, the electrical efficiency varies with incident solar irradiance, ambient temperature, and wind speed. Figure 11 shows how the ambient temperature varies as a function of the time of day at each location under study. Therefore, the electrical efficiency can take a large number of values. The electrical efficiency of *PV* cells was considered to be the same for both technologies, i.e., 0.18. The operating temperature of the *PV* cells was also assumed to be the same. It can be considered that the losses Q_{convPV} and Q_{radPV} remain constant if the solar irradiance remains constant.
(iii) The *NCPV* system has a southern orientation and an optimal tilt angle, as determined by the procedure used in [62].
(iv) The method proposed by [60] was used to determine solar irradiance for both technologies.

Table 6 shows the optimum tilt angle and the annual solar irradiation incident on the *PV* cells of the *NCPV* system at each location under study.

Table 6. Results obtained for the NCPV system.

	Cities	Optimum Tilt Angle (°)	H_{NCPV} (kWh)
1	Medellin (Colombia)	4.5	950.39
2	Bangkok (Thailand)	13.2	1002.58
3	Morelia (Mexico)	19.9	1198.87
4	Karachi (Pakistan)	23.6	1265.54
5	Cairo (Egypt)	24.2	1293.05
6	Almeria (Spain)	30.3	1264.38

Figure 16 shows the solar irradiation gain incident on the *PV* cells according to the following equation:

$$HG = \frac{H_{NCPV} - H_{CPV}}{H_{NCPV}} \cdot 100 \quad (17)$$

where H_{NCPV} is the solar irradiation incident on the *PV* cells in the *NCPV* system (kWh), and H_{CPV} is the solar irradiation incident on the *PV* cells in the *CPV* system (kWh).

As with all *NCPV* systems, all three solar irradiance components are incident on the *PV* cells, and the incident solar irradiance will be much higher than in the case of *CPV* systems, which only use the beam component of the solar irradiance. As shown in Figure 23, the studied configuration always shows better results than the base configuration. With respect to the base configuration ($\beta_M = 0$ (°) and $\beta_S = 0$ (°)), the solar irradiation gain is higher than 60%, whereas it is higher than 45% for the longitudinal tilt configuration.

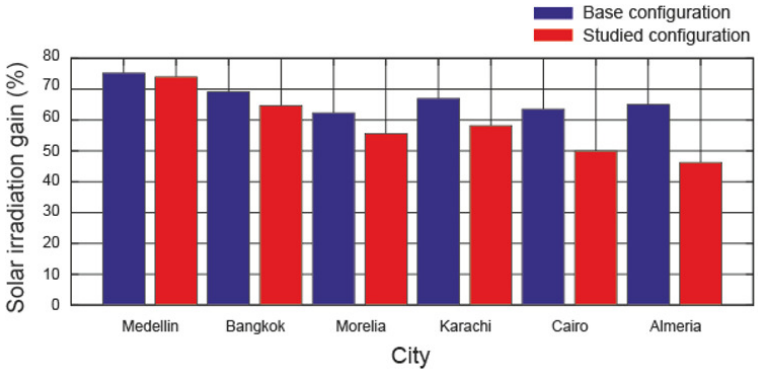

Figure 23. Solar irradiation gain incident on the photovoltaic cells.

The total useful energy in the *NCPV* system is only electrical energy. In contrast, the total useful energy in the *CPV* system is the sum of electrical energy and thermal energy. To compare the two technologies, the total useful energy gain must be used:

$$EG = \frac{E_{NCPV} - E_{CPV}}{E_{NCPV}} \cdot 100 \quad (18)$$

where E_{NCPV} is the total useful energy in the *NCPV* system (kWh), and E_{CPV} is the total useful energy in the *CPV* system (kWh). If *EG* is positive, *NCPV* systems prove to perform better; however, *CPV* systems are considered higher-performing if *EG* is negative. Figure 24 shows the total useful energy gain for the base configuration ($\beta_M = 0$ (°) and $\beta_S = 0$ (°)) and for the studied configuration.

The total useful energy gain at the lowest latitude location (Medellin) in the absence of wind (see Figure 24a) is in favour of *NCPV* systems. In contrast, this energy gain is in favour of *CPV* systems for higher latitudes. As in the rest of the work, the studied configuration shows better results than the base configuration. It is worth noting that this gain is 70% higher at the highest latitude location (Almeria) in the case of *CPV* systems. Figure 24b shows the effect of wind on the useful energy gain. If the wind speed

is 10.03 (m/s), the $NCPV$ systems perform much better. The energy gain of $NCPV$ systems decreases considerably with increasing latitude.

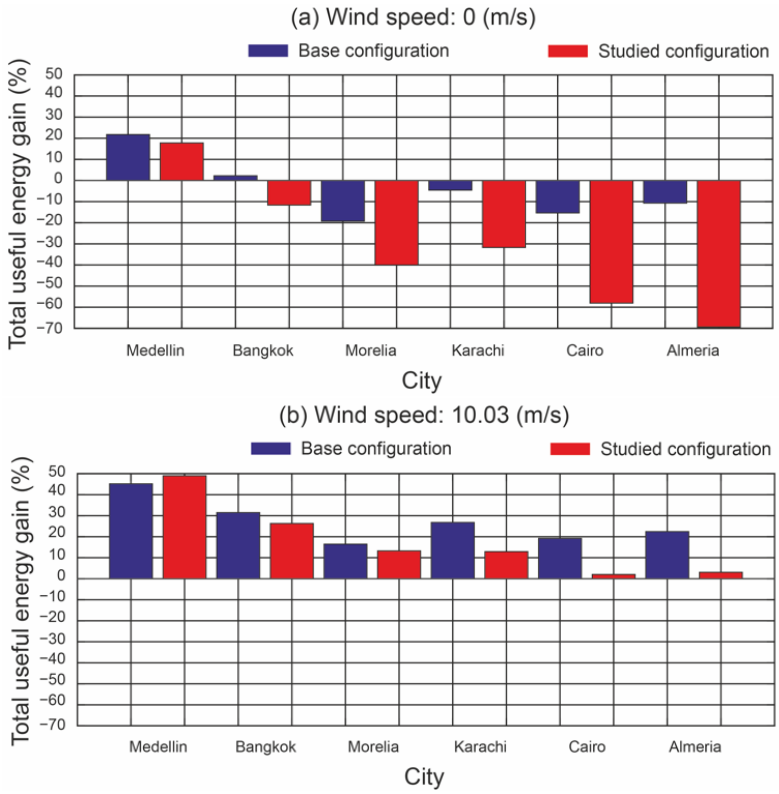

Figure 24. Total useful energy gain.

5. Conclusions

This paper experimentally studied the influence of a longitudinal tilt angle for the secondary system of a small-scale linear Fresnel reflector used in a low-concentrating photovoltaic system based on several evaluation indicators (useful heat gain, thermal efficiency) under various wind speed conditions and in different locations throughout the Northern Hemisphere. Other evaluation indicators were also analysed, such as solar irradiation gain incident on the photovoltaic cells and total useful energy gain. A comparative study between nonconcentrating and low-concentrating photovoltaic systems was also carried out. The experiments to obtain the evaluation indicators were carried out with two configurations: a base configuration and a longitudinal tilt configuration. The base configuration is the classical configuration of large-scale linear Fresnel reflectors and is characterised by $\beta_M = 0$ (°) and $\beta_S = 0$ (°). The basis of the study is the power not converted into electricity by the photovoltaic cells, i.e., the thermal power wasted in a nonconcentrated photovoltaic system. Depending on the dimensions of the prototype used, a resistor simulating the thermal power of 300 and 400 (W) was used. Therefore, this power takes into account the operating temperature of the photovoltaic cells. The longitudinal tilt configuration is characterised by the optimal longitudinal tilt angles [24] $\beta_M = \lambda/2$ (°) and $\beta_S = \lambda$ (°). The experiments were carried out with five wind speeds (around 0 (m/s), 1.05 (m/s), 2.55 (m/s), 4.99 (m/s), and 10.03 (m/s)), and six cities in the Northern Hemisphere (Medellin, Bangkok, Morelia, Karachi, Cairo, and Almeria). To carry out the research, an experimental platform was designed and built, consisting of the secondary system of a small-scale linear Fresnel reflector, an open-loop wind tunnel, an electrical subsystem, a thermal subsystem, a longitudinal tilt system of the secondary system, and measuring equipment. The following conclusions were drawn:

(i) As concerns useful heat production, the longitudinal tilt configuration performs worse as the longitudinal tilt angle and wind speed increase. For example, the following is

true for the power not converted into electricity by the photovoltaic cells of 400 (W): (a) When the wind speed is 10.03 (m/s), the useful heat gain shows the worst results, ranging from −21.30% (Medellin) to −33.91% (Almeria). (b) If the wind speed drops below this value, e.g., 4.99 (m/s), the useful heat gain also decreases, resulting in useful heat gains between −17.27% (Medellín) and −18.77% (Almería). (c) For 2.55 (m/s), the useful heat gain is approximately −8%. (d) When the wind speed is 0 (m/s), the useful heat in the longitudinal tilt configuration is similar to that of the base configuration. As wind speed increases, the difference in useful heat gain between lower and higher latitude locations increases.

(ii) The thermal efficiency decreased with increasing wind speed and a longitudinal tilt angle. The thermal efficiency was always below 0.6. As wind speed increases, this value decreases. This effect is more pronounced as the longitudinal tilt angle increases. For example, the following is true for the power not converted into electricity by the photovoltaic cells of 400 (W): (a) When the wind speed is 1.05 (m/s), the thermal efficiency ranges between 0.5 and 0.4. (b) For wind speeds of 2.55 (m/s), it ranges between 0.4 and 0.3. (c) For wind speeds of 4.99 (m/s) and 10.03 (m/s), the thermal efficiency is between 0.3 and 0.2. The lowest thermal efficiency is obtained in Almeria (location with the highest latitude).

(iii) The total useful energy in a low-concentration photovoltaic system is the sum of the electrical energy generated and the useful thermal energy produced. The longitudinal tilt configuration shows the best increase in total useful energy in the absence of wind. The lowest latitude site (Medellín) has the lowest increase. On the other hand, for higher latitudes, this total useful energy gain takes values up to 53% (Almeria). The longitudinal tilt configuration remains the best-performing when the wind speed is 10.03 (m/s), except for the lowest latitude location (Medellin). At this wind speed, the total useful energy gain decreases to 25% for the highest latitude location (Almeria). Therefore, it can be concluded that secondary system designs with longitudinal tilt angles perform well at locations with latitudes above 10 (°). These results are very good if the latitude is higher than 24 (°) and lower than 37 (°). It can be concluded that the effect of the longitudinal tilt of the secondary system has a positive effect.

To highlight the importance of this work, the results obtained in the configuration comparison were used to compare a nonconcentrating photovoltaic system and a low-concentrating photovoltaic system. The following conclusions were drawn: (i) The solar irradiance incident on the photovoltaic cells will be much higher in nonconcentrating photovoltaic technology. This solar irradiance gain is more than 60% with the base configuration and 45% with the longitudinal tilt configuration. (ii) The total useful energy gain at the lowest latitude location (Medellín) is the only location favourable to nonconcentrating photovoltaic systems in the absence of wind. For all other locations, this gain is in favour of low-concentrating photovoltaic systems. It is worth noting that this gain is −70% at the highest latitude location (Almeria). (iii) The nonconcentrating photovoltaic system performs better if the wind speed is 10.03 (m/s). With increasing latitude, the total useful energy gain of the nonconcentrating photovoltaic system decreases considerably.

Author Contributions: Conceptualization, C.L.-S., A.B. and L.B.; methodology, A.B. and L.B.; software, C.L.-S. and C.B.-C.; validation, A.B. and L.B.; investigation, C.L.-S. and C.B.-C.; data curation, C.L.-S. and C.B.-C.; writing—original draft, C.L.-S. and C.B.-C.; writing—review and editing, C.L.-S. and C.B.-C. All authors have read and agreed to the published version of the manuscript.

Funding: This research received no external funding.

Data Availability Statement: The original contributions presented in the study are included in the article, further inquiries can be directed to the corresponding author.

Conflicts of Interest: Author Covadonga Bayón-Cueli was employed by the company DNV UK Limited, OPEX. The remaining authors declare that the research was conducted in the absence of any commercial or financial relationships that could be construed as a potential conflict of interest.

Nomenclature

A_{AC}	Area of the flat tube (m^2)
A_{PV}	Total area of the PV cells (m^2)
C_p	Heat capacity of the water (J/kg° C)
CL_g	Cleanliness factor of the glass (*dimensionless*)
CL_m	Cleanliness factor of the mirror (*dimensionless*)
D_h	Hydraulic diameter of the flat tube (m)
d_i	Separation between $i-th$ and $i+1-th$ mirrors (m)
EG	Total useful energy gain (*dimensionless*)
E_C	Total useful energy in a configuration (kWh)
E_{CPV}	Total useful energy in CPV system (kWh)
E_{NCPV}	Total useful energy in $NCPV$ system (kWh)
e_R	Overall uncertainty associated with the measurement (%)
f	Height of the receiver (m)
HG	Solar irradiation gain (*dimensionless*)
H_B	Beam solar irradiation incident (kWh)
H_{CPV}	Solar irradiation incident on the PV cells (kWh)
H_{NCPV}	Solar irradiation incident on the PV cells (kWh)
I_t	Total absorbed solar irradiance for PV system (W/m^2)
k	Thermal conductivity (W/m° C)
L_i	Position of $i-th$ mirror (m)
L_{AC}	Length of the active cooling system (m)
L_M	Length of the mirrors (m)
L_{PV}	Length of the PV system (m)
m	Fluid mass flow rate (kg/s)
N	Number of mirrors on each side of the SSLFR
P_{rw}	Prandtl number of the working fluid (*dimensionless*)
Q_{cond}	Conduction heat transfer (W)
Q_{conv}	Convection heat transfer (W)
Q_{rad}	Radiation heat transfer (W)
Q_{th}	Internal heat generation in PV cells (W)
Q_u	Useful heat (W)
R_{ew}	Reynolds number of the working fluid (*dimensionless*)
T_{amb}	Ambient temperature (°C)
T_{AC}	Temperature of the flat tube (°C)
T_{PV}	Temperature of the PV cells (°C)
T_{in}	Temperature of the inlet fluid to the secondary system (°C)
T_{out}	Temperature of the outlet fluid to the secondary system (°C)
T_{ref}	Reference temperature (°C)
T_w	Working fluid temperature (°C)
UHG	Useful heat gain (*dimensionless*)
W_{AC}	Width of the active cooling system (m)
W_{Mi}	Width of the $i-th$ mirror (m)
W_{PV}	Width of the PV cells (m)
α	Absorptivity of the PV cell (*dimensionless*)
β_i	Angle which mirror i forms with the horizontal (°C)
β_M	Angle between the mirror axis and the horizontal plane (°C)
β_{ref}	Temperature coefficient (1/°C)
β_S	Angle between the PV system and the horizontal plane (°C)
δ_{AC}	Wall thickness of the flat tube (m)
η_e	Electrical efficiency of the PV system (*dimensionless*)
η_{ref}	Reference electrical efficiency (*dimensionless*)
η_{th}	Thermal efficiency (*dimensionless*)
θ_i	Angle between the vertical and the line centre point of each mirror with the focal point (°)
θ_l	Longitudinal incidence angle (°C)
θ_t	Transversal incidence angle (°C)
θ_{t_0}	Operation interval (°C)

λ	Latitude (°C)
ρ	Reflectivity of the primary mirrors (*dimensionless*)
τ_e	Transmissivity of encapsulant (*dimensionless*)
τ_g	Transmissivity of glass (*dimensionless*)

References

1. Paris Agreement. In Proceedings of the Report of the Conference of the Parties to the United Nations Framework Convention on Climate Change (21st Session), Paris, Fance, 30 November–13 December 2015.
2. *Statistical Review of World Energy*, 72nd ed.; 2023. Available online: https://www.energyinst.org/statistical-review/resources-and-data-downloads (accessed on 20 June 2023).
3. Alzahrani, M.; Shanks, K.; Mallick, T.K. Advances and limitations of increasing solar irradiance for concentrating photovoltaics thermal system. *Renew. Sustain. Energy Rev.* **2021**, *138*, 110517. [CrossRef]
4. IRENA. Future of Solar Photovoltaic: Deployment, Investment, Technology, Grid Integration and Socio-Economic Aspects. International Renewable Energy Agency. 2019. Available online: https://www.irena.org/publications/2019/Nov/Future-of-Solar-Photovoltaic (accessed on 11 June 2023).
5. Huang, M.; Wang, Y.; Li, M.; Keovisar, V.; Li, X.; Kong, D.; Yu, Q. Comparative study on energy and exergy properties of solar photovoltaic/thermal air collector based on amorphous silicon cells. *Appl. Thermal Eng.* **2021**, *185*, 116376. [CrossRef]
6. Darkwa, J.; Calautit, J.; Du, D.; Kokogianakis, G. A numerical and experimental analysis of an integrated TEG-PCM power enhancement system for photovoltaic cells. *Appl. Energy* **2019**, *248*, 688–701. [CrossRef]
7. Poulek, V.; Šafránková, J.; Cerná, L.; Libra, M.; Beránek, V.; Finsterle, T.; Hrzina, P. PV panel and PV inverter damages caused by combination of edge delamination, water penetration, and high string voltage in moderate climate. *IEEE J. Photovoltaics* **2021**, *11*, 561–565. [CrossRef]
8. Kamath, H.G.; Ekins-Daukes, N.J.; Araki, K.; Ramasesha, S.K. The potential for concentrator photovoltaics: A feasibility study in India. *Prog. Photovoltaics Res. Appl.* **2018**, *27*, 316–327. [CrossRef]
9. Moreno, A.; Chemisana, D.; Fernández, E.F. Hybrid high-concentration photovoltaic-thermal solar systems for building applications. *Appl. Energy* **2021**, *304*, 117647. [CrossRef]
10. IRENA; IEA. End-of-Life Management: Solar Photovoltaic Panels. International Renewable Energy Agency and International Energy Agency Photovoltaic Power Systems. 2016. Available online: https://www.irena.org/publications/2016/Jun/End-of-life-management-Solar-Photovoltaic-Panels (accessed on 11 June 2023).
11. Vellini, M.; Gambini, M.; Stilo, T. High-efficiency cogeneration systems for the food industry. *J. Clean. Prod.* **2020**, *260*, 121133. [CrossRef]
12. Silva, R.M.; Fernandes, J.L.M. Hybrid photovoltaic/thermal (PV/T) solar systems simulation with Simulink/Matlab. *Sol. Energy* **2010**, *84*, 1985–1996. [CrossRef]
13. Tian, M.; Su, Y.; Zheng, H.; Pei, G.; Li, G.; Riffat, S. A review on the recent research progress in the compound parabolic concentrator (CPC) for solar energy applications. *Renew. Sustain. Energy Rev.* **2018**, *82*, 1272–1296. [CrossRef]
14. Barbón, A.; Fortuny Ayuso, P.; Bayón, L.; Fernández-Rubiera, J.A. Non-uniform illumination in low concentration photovoltaic systems based on smallscale linear Fresnel reflectors. *Energy* **2022**, *239*, 122217. [CrossRef]
15. Ghodbane, M.; Said, Z.; Amine Hachicha, A.; Boumeddane, B. Performance assessment of linear Fresnel solar reflector using MWCNTs/DW nanofluids. *Renew. Energy* **2020**, *151*, 43–56. [CrossRef]
16. Wang, G.; Chen, Z.; Hu, P.; Cheng, X. Design and optical analysis of the band-focus Fresnel lens solar concentrator. *Appl. Therm.* **2016**, *102*, 695–700. [CrossRef]
17. Wang, G.; Yao, Y.; Chen, Z.; Hu, P. Thermodynamic and optical analyses of a hybrid solar CPV/T system with high solar concentrating uniformity based on spectral beam splitting technology. *Energy* **2019**, *166*, 256–266. [CrossRef]
18. Wang, K.-J.; Yang J.-W. Sunlight concentrator design using a revised genetic algorithm. *Renew. Energy* **2014**, *72*, 322–335. [CrossRef]
19. Wang, G.; Wang, F.; Shen, F.; Jiang, T.; Chen, Z.; Hu, P. Experimental and optical performances of a solar CPV device using a linear Fresnel reflector concentrator. *Renew. Energy* **2020**, *146*, 2351–2361. [CrossRef]
20. Wang, G.; Chen, Z.; Hu, P. Design and experimental investigation of a multi-segment plate concentrated photovoltaic solar energy system. *Appl. Therm. Eng.* **2017**, *116*, 147–152. [CrossRef]
21. Jiang, S.; Hu, P.; Mo, S.; Chen, Z. Optical modeling for a two-stage parabolic trough concentrating photovoltaic/thermal system using spectral beam splitting technology. *Sol. Energy Mater. Sol. Cells* **2010**, *94*, 1686–1696. [CrossRef]
22. Barbón, A.; Barbón, N.; Bayón, L.; Sánchez-Rodríguez, J.A. Parametric study of the small-scale linear Fresnel reflector. *Renew. Energy* **2018**, *116*, 64–74. [CrossRef]
23. Barbón, A.; Bayón-Cueli, C.; Bayón, L.; Rodríguez, L. Investigating the influence of longitudinal tilt angles on the performance of small scale linear Fresnel reflectors for urban applications. *Renew. Energy* **2019**, *143*, 1581–1593. [CrossRef]
24. Barbón, A.; Bayón-Cueli, C.; Fernández-Rubiera, J.A.; Bayón, L. Theoretical deduction of the optimum tilt angles for small-scale linear Fresnel reflectors. *Energies* **2021**, *14*, 2883. [CrossRef]
25. Barbón, A.; López-Smeetz, C.; Bayón, L.; Pardellas, A. Wind effects on heat loss from a receiver with longitudinal tilt angle of small-scale linear Fresnel reflectors for urban applications. *Renew. Energy* **2020**, *162*, 2166–2181. [CrossRef]

26. Barbón, A.; Fernández-Rubiera, J.A.; Martínez-Valledor, L.; Pérez-Fernández, A.; Bayón, L. Design and construction of a solar tracking system for small-scale linear Fresnel reflector with three movements. *Appl. Energy* **2021**, *285*, 116477. [CrossRef]
27. Morin, G.; Dersch, J.; Platzer, W.; Eck, M.; Häberle, A. Comparison of linear Fresnel and parabolic trough collector power plants. *Sol. Energy* **2012**, *86*, 1–12. [CrossRef]
28. Barbón, A.; Bayón, L.; Bayón-Cueli, C.; Barbón, N. A study of the effect of the longitudinal movement on the performance of small-scale linear Fresnel reflectors. *Renew. Energy* **2019**, *138*, 128–138. [CrossRef]
29. Li , G.; Xuan, Q.; Pei, G.; Su, Y.; Ji, J. Effect of non-uniform illumination and temperature distribution on concentrating solar cell—A review. *Energy* **2018**, *144*, 1119–1136. [CrossRef]
30. Guerriero, P.; Tricoli, P.; Daliento, S. A bypass circuit for avoiding the hot spot in PV modules. *Sol. Energy* **2019**, *181*, 430–438. [CrossRef]
31. Shi, S.; Zhang, D.; Bi, L.; Ding, R.; Ren, W.; Tang, X.; He, Y. Enhancement of thermal conductivity and insulation of silicone thermal interface material through surface modification and synergistic effects of nanofillers for thermal management of electronic devices. *Diam. Relat. Mater.* **2024**, *145*, 111064. [CrossRef]
32. RD. Available online: https://es.rs-online.com/web/p/grasa-termica/0554311 (accessed on 15 April 2024).
33. Zhu, Y.; Shi, J.; Li, Y.; Wang, L.; Huang, Q.; Xu, G. Design and thermal performances of a scalable linear Fresnel reflector solar system. *Energy Convers. Manag.* **2017**, *146*, 174–181. [CrossRef]
34. Zhu, Y.; Shi, J.; Li, Y.; Wang, L.; Huang, Q.; Xu, G. Design and experimental investigation of a stretched parabolic linear Fresnel reflector collecting system. *Energy Convers. Manag.* **2016**, *126*, 89–98. [CrossRef]
35. Barbón, A.; Sánchez-Rodríguez, J.A.; Bayón, L.; Bayón-Cueli, C. Cost estimation relationships of a small scale linear Fresnel reflector. *Renew. Energy* **2019**, *134*, 1273–1284. [CrossRef]
36. Fernández-Rubiera, J.A.; Barbón, A.; Bayón, L.; Ghodbane, M. Sawtooth V-trough cavity for low concentration photovoltaic systems based on small-scale linear Fresnel reflectors: Optimal design, verification and construction. *Electronics* **2023**, *12*, 2770. [CrossRef]
37. Duffie, J.A.; Beckman, W.A. *Solar Engineering of Thermal Processes*, 4th ed.; John Wiley & Sons: New York, NY, USA, 2013.
38. Sharma, V.M.; Nayak, J.K.; Kedare, S.B. Effects of shading and blocking in linear Fresnel reflector field. *Sol. Energy* **2015**, *113*, 114–138. [CrossRef]
39. Theunissen, P.H.; Beckman, W.A. Solar transmittance characteristics of evacuated tubular collectors with diffuse back reflectors. *Sol. Energy* **1985**, *35*, 311–320. [CrossRef]
40. Kohan, H.R.F.; Lotfipour, F.; Eslami, M. Numerical simulation of a photovoltaic thermoelectric hybrid power generation system. *Sol. Energy* **2018**, *174*, 537–548. [CrossRef]
41. Giffith, B.; Torcellini, P.; Long, N. *Assessment of the Technical Potential for Achieving Zero-Energy Commercial Buildings*; ACEEE Summer Study Pacific Grove; National Renewable Energy Lab, (NREL): Golden, CO, USA, 2006.
42. *ISO 9806:2017*; Solar Energy—Solar Thermal Collectors—Test Methods. ISO: Geneva, Switzerland, 2017.
43. Herrando, M.; Ramos, A.; Zabalza, I.; Markides, C.N. A comprehensive assessment of alternative absorber-exchanger designs for hybrid PVT-water collectors. *Appl. Energy* **2019**, *235*, 1583–1602. [CrossRef]
44. Kalogirou, S.A.; Agathokleous, R.; Barone, G.; Buonomano, A.; Forzano, C.; Palombo, A. Development and validation of a new TRNSYS Type for thermosiphon flat-plate solar thermal collectors: Energy and economic optimization for hot water production in different climates. *Renew. Energy* **2019**, *136*, 632–644. [CrossRef]
45. MATRIX. Available online: https://www.ujaen.es/departamentos/ingele/sites/departamento_ingele/files/uploads/manualwatimetrodigitalPX110.PDF (accessed on 18 August 2023).
46. TESTO. Available online: https://www.testo.com/en/ (accessed on 18 August 2023).
47. AICHITOKEI. Available online: https://www.aichitokei.net/products/microflow-sensor-of-z/ (accessed on 18 August 2023).
48. Li, M.; Zhang, Q.; Li, G.; Shao, S. Experimental investigation on performance and heat release analysis of a pilot ignited direct injection natural gas engine. *Energy* **2015**, *90*, 1251–1260. [CrossRef]
49. Rahman, M.M.; Hamada, K.I.; Aziz, A.R.A. Characterization of the timeaveraged overall heat transfer in a direct-injection hydrogen-fueled engine. *Int. J. Hydrog. Energy* **2013**, *38*, 4816–4830. [CrossRef]
50. Al-Waeli , A.H.A.; Chaichan, M.T.; Sopian, K.; Kazem, H.A.; Mahood, H.B.; Khadom, A.A. Modeling and experimental validation of a PVT system using nanofluid coolant and nano-PCM. *Sol. Energy* **2019**, *177*, 178–191. [CrossRef]
51. UN. World Population Prospects 2019. United Nations **2019**. Available online: https://population.un.org/wpp/ (accessed on 6 March 2023).
52. Odyssee-Mure, Energy Efficiency Trends in Buildings in the EU Lessons from the ODYSSEE MURE Project, 2015. Available online: http://www.odyssee-mure.eu/publications/br/energy-efficiency-trends-policies-buildings.pdf (accessed on 6 March 2021).
53. SOLARGIS. Available online: https://solargis.com/maps-and-gis-data/download/world (accessed on 20 June 2023).
54. PVGIS. Joint Research Centre (JRC). Available online: http://re.jrc.ec.europa.eu/pvg_tools/en/tools.html#PVP (accessed on 11 June 2023).
55. Aly, S.P.; Ahzi, S.; Barth, N.; Abdallah, A. Using energy balance method to study the thermal behavior of PV panels under time-varying field conditions. *Energy Convers. Manag.* **2018**, *175*, 246–262. [CrossRef]
56. Cengel, Y.A. *Heat Transfer and Mass Transfer: A Practical Approach*, 3rd ed.; McGraw Hill Book Company: New York, NY, USA, 2006.

57. Guarracino, I.; Mellor, A.; Ekins-Daukes, N.J.; Markides, C.N. Dynamic coupled thermal-and-electrical modelling of sheet-and-tube hybrid photovoltaic/thermal (PVT) collectors. *Appl. Therm. Eng.* **2016**, *101*, 778–795. [CrossRef]
58. Evans, D.L. Simplified method for predicting photovoltaic array output. *Sol. Energy* **1981**, *27*, 555–560. [CrossRef]
59. Mills, A.F. *Heat Transfer*, 2nd ed.; Prentice Hall: Upper Saddle River, NJ, USA, 2005.
60. Barbón, A.; Fortuny Ayuso, P.; Bayón, L.; Fernández-Rubiera, J.A. Predicting beam and diffuse horizontal irradiance using Fourier expansions. *Renew. Energy* **2020**, *154*, 46–57. [CrossRef]
61. Mattei, M.; Notton, G.; Cristofari, C.; Muselli, M.; Poggi, P. Calculation of the polycrystalline PV module temperature using a simple method of energy balance. *Renew. Energy* **2006**, *31*, 553–567. [CrossRef]
62. Jacobson, M.Z.; Jadhav, V. World estimates of PV optimal tilt angles and ratios of sunlight incident upon tilted and tracked PV panels relative to horizontal panels. *Sol. Energy* **2018**, *169*, 55–66. [CrossRef]

Disclaimer/Publisher's Note: The statements, opinions and data contained in all publications are solely those of the individual author(s) and contributor(s) and not of MDPI and/or the editor(s). MDPI and/or the editor(s) disclaim responsibility for any injury to people or property resulting from any ideas, methods, instructions or products referred to in the content.